Geophysical Journal International

Geophys. J. Int. (2014) **199,** 1138–1160
GJI Seismology

doi: 10.1093/gji/ggu319

Kinematic earthquake rupture inversion in the frequency domain

Wenyuan Fan, Peter M. Shearer and Peter Gerstoft

Scripps Institution of Oceanography, University of California, San Diego, 9500 *Gilman Drive, La Jolla, CA* 92093, *USA. E-mail: w3fan@ucsd.edu*

Accepted 2014 August 14. Received 2014 August 12; in original form 2014 April 4

SUMMARY

We develop a frequency-based approach to earthquake slip inversion that requires no prior information on the rupture velocity or slip-rate functions. Because the inversion is linear and is performed separately at each frequency, it is computationally efficient and suited to imaging the finest resolvable spatial details of rupture. We demonstrate the approach on synthetic seismograms based on the Source Inversion Validation Exercise 1 (SIV1) of a crustal M_w 6.6 strike-slip earthquake recorded locally. A robust inversion approach is obtained by applying a combination of damping, smoothing and forcing zero slip at the edge of the fault model. This approach achieves reasonable data fits, overall agreement to the SIV1 model, including slip-rate functions of each subfault, from which its total slip, slip time history and rupture velocity can be extracted. We demonstrate the method's robustness by exploring the effects of noise, random timing errors, and fault geometry errors. The worst effects on the inversion are seen from errors in the assumed fault geometry.

Key words: Fourier analysis; Inverse theory; Earthquake ground motions; Earthquake source observations.

1 INTRODUCTION

Kinematic finite-slip inversion resolves the spatiotemporal behaviour of the rupture process during an earthquake. It generally does not directly require the resolved slip to be physically or dynamically plausible, although often constraints inferred from earthquake physics are applied to kinematic inversions. Various geophysical data can be used in kinematic studies, including seismic (Yagi & Fukahata 2011), geodetic (Tong *et al.* 2010), tsunami (Yokota *et al.* 2011) and borehole records (Koketsu *et al.* 2004). Kinematic finite-slip models describe the whole rupture process, including its dimensions and rupture velocity, and help in understanding the conditions for pulse-like ruptures and super-shear ruptures. They provide clues regarding spatial variations in stress drop and fault asperities, while providing real-world constraints on dynamic rupture models and studies of earthquake physics (e.g. Causse *et al.* 2014). See Ide (2007) for a recent review of finite-slip inversion methods.

The first heterogeneous finite-slip inversion was Trifunac (1974), in which the fault plane was divided into several subfaults and the slip of each subfault was estimated as a Haskell model (Haskell 1969). The key idea was to construct the fault plane as a set of subfaults and modern finite-slip inversion approaches continue to adopt this parametrization. Important early work includes Olson & Apsel (1982) and Hartzell & Heaton (1983), who developed a linear inversion method with inequality constraints to determine the spatial and temporal slip distribution of the 1979 Imperial Valley earthquake. The method and its extension are referred to as the multi-time-window method, which have been widely applied (e.g. Yagi 2004; Uchide *et al.* 2009; Yue *et al.* 2012). More recently, Ji *et al.* (2002) adopted the Meyer–Yamada wavelet transform and simulated annealing algorithm to determine the finite-fault model that minimizes an objective function described in terms of wavelet coefficients, and applied it to the 1999 Hector Mine earthquake. Other nonlinear approaches, like Bayesian inversion, have been enabled by rapid improvements of computing power (e.g. Monelli & Mai 2008; Monelli *et al.* 2009; Minson *et al.* 2013, 2014; Dettmer *et al.* 2014). Without assumptions about slip rate function shape or rupture velocity, solving source time functions in the time domain is a huge inverse problem, a multidimensional deconvolution problem. It can be simplified and made more computationally tractable by using source–time functions with idealized shapes.

Because ruptures do not necessarily have simple slip functions or constant rupture velocities, it is desirable to develop methods that make few assumptions about the model. For computational reasons, this is more likely possible in the frequency domain where the multidimensional deconvolution is replaced with solving a linear set of equations for each frequency (Olson & Anderson 1988; Mendez & Anderson 1991; Cotton & Campillo 1995). Here we describe and further develop a frequency-domain algorithm for finite-slip inversion. For each frequency, the seismic velocity spectrum is a linear superposition of the Green's functions multiplied by the slip-rate spectra on each subfault. Since this set of equations is solved independently at each frequency, the complexity of the inverse problem is greatly reduced. This computational efficiency enables dense parametrization of the subfaults for good spatial resolution and we avoid assuming a rupture velocity or specific form for the source–time function, which might limit the ability to resolve complex rupture models. To stabilize the inversion, regularization is applied instead.

The frequency domain approach follows Olson & Anderson (1988), but with the following improvements: (1) we derive and apply Bayesian based regularizations which penalize variations in the inverted slip-rate functions, including ℓ_2 norm, roughness and ℓ_1 norm (i.e. compressive sensing, which produces sparse models), (2) we consider larger problems (e.g. more fault patches), exploiting improved computer resources and recently developed convex optimization approaches for solving the inverse problem (Boyd & Vandenberghe 2004).

Finite slip inversions are now performed routinely and are often available within a few days after an earthquake. However, understanding the uniqueness of these solutions remains challenging (e.g. Vallée & Bouchon 2004; Shao & Ji 2012; Konca *et al.* 2013; Razafindrakoto & Mai 2014). Fault geometry parametrization, assumed Earth structure, seismic data type, Green's function calculation methods, inversion approaches and regularization constraints all affect the inversion results. Thus, rupture models often show substantial variations among different groups, even while fitting the data equally well. There are no generally accepted criteria to evaluate the available models and their uncertainties, making interpreting the inverted models inherently subjective. Aiming to quantify the uncertainty in earthquake source inversion, the source inversion validation (SIV) project (Mai *et al.* 2007) provides an online cooperative platform to test earthquake source inversion approaches through a series of benchmarks.

To test our frequency-domain method, we apply it to SIV Exercise 1 (SIV1, near-vertical strike-slip fault, recorded locally). We do not prescribe the rupture velocity and slip-rate functions, but apply regularization to stabilize the inversion, as we overparametrize the model to avoid bias from too few unknowns. To provide good spatiotemporal resolution, subfaults are 1 km × 1 km and the slip-rate spectra are fit up to 1 Hz. We experiment with a variety of physically plausible regularization constraints to stabilize the inversion.

In the following sections, we will describe our method and explore the effects of inversion constraints, regularization strengths, noise and fault geometry. Our results for the SIV1 show that even with perfectly known Green's functions, noise-free data, and a good station distribution, a wide variety of fault-slip models provide good fits to the data. The finite-slip inversion problem is inherently nonunique and regularization is necessary to obtain a stable result. However, because different regularizations produce different models, choosing the most appropriate regularization is critical and the best regularization strategy will vary depending on the details of each inversion problem.

2 THEORY

In the frequency domain, the slip-rate spectra and recorded strong-motion spectra are linked by a linear Green's function relationship. The spatial unknowns for each subfault patch can be inverted independently for each frequency. The problem can be solved efficiently in this fashion without any rupture time restriction (Olson & Anderson 1988). The increased efficiency allows finer discretization of subfaults, which gives the inverted rupture model greater resolution to resolve rapid spatial changes. The approach avoids subjective decisions about the slip-rate function shape and rupture velocity and eliminates the trade-off between rupture velocity and rupture front. In this section, we start with a brief review of the forward modelling approach. Using the same fault geometry as in forward modelling, we then construct and perform inversions with various constraints in the frequency domain. Finally, a time-domain misfit function is applied to comprehensively compare data misfit.

2.1 Model setup and forward modelling

Using the representation theorem, (e.g. Aki & Richards 2002), the recorded displacement can be expressed as the convolution of the Green's function of the source-receiver pair and the discontinuity displacement across the fault plane. There is a linear relationship in the frequency domain between the recorded displacement spectrum and the source displacement spectrum. Thus, the recorded velocity spectrum is linearly linked to the slip-rate spectrum by the Green's function. Using this linear relationship, we modify eq. (15) of Spudich & Archuleta (1987) into a discrete form:

$$v_i(\mathbf{x}, f) = \sum_j^M \left(T_i^s(\mathbf{x}, f; \boldsymbol{\xi}^j) \quad T_i^d(\mathbf{x}, f; \boldsymbol{\xi}^j) \right) \begin{pmatrix} [v^s(\boldsymbol{\xi}^j, f)] \\ [v^d(\boldsymbol{\xi}^j, f)] \end{pmatrix} \triangle\Sigma(\boldsymbol{\xi}^j), \tag{1}$$

where the ith component of ground velocity spectrum $v_i(\mathbf{x}, f)$ at the Earth's surface $\mathbf{x}$ and frequency f is expressed as a multiple of the traction and a slip-rate discontinuity across the fault plane. The fault plane is modelled as a set of M subfaults. Here $[v^s(\boldsymbol{\xi}^j, f)]$ and $[v^d(\boldsymbol{\xi}^j, f)]$ are the strike-slip and dip-slip slip-rate spectra at the jth subfault $\boldsymbol{\xi}^j$; $T_i^s(\mathbf{x}, f; \boldsymbol{\xi}^j)$ and $T_i^d(\mathbf{x}, f; \boldsymbol{\xi}^j)$ are the strike-slip and dip-slip tractions exerted with respect to the receiver and subfault setting; and $\triangle\Sigma(\boldsymbol{\xi}^j)$ is the subfault area at $\boldsymbol{\xi}^j$. The synthetic seismogram $v_i(\mathbf{x}, t)$ is obtained by taking the inverse Fourier transform of the velocity spectrum $v_i(\mathbf{x}, f)$.

2.2 Inverse formulation

To set up the inverse problem, we first Fourier transform the observed seismograms and align them into a vector according to station index, obtaining $\mathbf{d}^o(f) \in \mathbb{C}^{3N}$, where N is station number and each station has three components (x, y and z). The problem is thus expressed as

$$\mathbf{d}^o(f) = [\mathbf{G}^s \quad \mathbf{G}^d] \begin{bmatrix} \mathbf{m}^s(f) \\ \mathbf{m}^d(f) \end{bmatrix} + \mathbf{n}(f) = \mathbf{G}\mathbf{m} + \mathbf{n}(f), \tag{2}$$

where vectors $\mathbf{m}^s(f) \in \mathbb{C}^M$ and $\mathbf{m}^d(f) \in \mathbb{C}^M$ are the strike-slip and dip-slip slip-rate spectral components. Matrices $\mathbf{G}^s \in \mathbb{C}^{3N\times M}$ and $\mathbf{G}^d \in \mathbb{C}^{3N\times M}$ are the Green's function matrices linking the source spectra and the recording spectra. G^s_{ij} and G^d_{ij} are the media responses of the ith recording due to strike-slip and dip-slip slip-rate pulses at subfault j, where $G^s_{ij} = T_i^s(\mathbf{x}, f; \boldsymbol{\xi}^j)\triangle\Sigma(\boldsymbol{\xi}^j)$ and $G^d_{ij} = T_i^d(\mathbf{x}, f; \boldsymbol{\xi}^j)\triangle\Sigma(\boldsymbol{\xi}^j)$. Differences between observations and synthetic seismograms from source models are described as noise $\mathbf{n}$, which contains both data noise and any errors due to forward modelling. The inversion is performed at each frequency independently, which greatly reduces the problem size (Olson & Anderson 1988). Note that the time and frequency parametrizations are physically equivalent, and thus identical solutions should be possible in either domain (Spudich & Archuleta 1987).

2.3 Objective functions

We tackle the problem using a Bayesian approach:

$$p(\mathbf{m}|\mathbf{d}^o) = \frac{p(\mathbf{d}^o|\mathbf{m})p(\mathbf{m})}{p(\mathbf{d}^o)}, \tag{3}$$

where $p(\mathbf{m})$ is the prior model probability density function (PDF), $\mathbf{d}^o$ is the observed data and $p(\mathbf{d}^o|\mathbf{m})$ is the conditional PDF. Maximizing $p(\mathbf{m}|\mathbf{d}^o)$, we obtain the maximum *a posteriori* (MAP) solution:

$$\hat{\mathbf{m}} = \arg\max_{\mathbf{m}} p(\mathbf{m}|\mathbf{d}^o). \tag{4}$$

2.3.1 Least squares

Assume $\mathbf{n}$ in eq. (2) obeys a complex Gaussian distribution, $\mathcal{C}N(\mathbf{0}, \sigma^2\mathbf{W}^{-1})$. Then the likelihood function can be expressed as

$$p(\mathbf{d}^o|\mathbf{m}) = c_0 \exp\left[-\frac{1}{\sigma^2}(\mathbf{d}^o - \mathbf{G}\mathbf{m})^{\mathrm{H}}\mathbf{W}(\mathbf{d}^o - \mathbf{G}\mathbf{m})\right]. \tag{5}$$

The constraints come in via the prior distribution $p(\mathbf{m})$, since the $p(\mathbf{d}^o)$ is just a normalizing constant. In the following sections, we derive several regularization approaches and other priors can be easily utilized. The simplest prior model distribution is a non-informative uniform distribution, in which case, eq. (4) gives the least-squares solution:

$$\begin{aligned}\hat{\mathbf{m}} &= \arg\max_{\mathbf{m}} c_0 \exp\left[-\frac{1}{\sigma^2}(\mathbf{d}^o - \mathbf{G}\mathbf{m})^{\mathrm{H}}\mathbf{W}(\mathbf{d}^o - \mathbf{G}\mathbf{m})\right] \\ &= \arg\min_{\mathbf{m}} \|\mathbf{d}^o - \mathbf{G}\mathbf{m}\|^2_{\mathbf{W},2},\end{aligned} \tag{6}$$

where c_0 is a constant and the covariance matrix is $\mathbf{W}^{-1}$, which can be treated as a weighting matrix for the recorded data with respect to site effects and data quality. When $\mathbf{n}$ is assumed to be identical and independent, $\mathbf{W}$ is the identity matrix $\mathbf{I}$. The objective function (6) of the weighted least squares problem is (convex) quadratic, which is a quadratic program (QP) problem (Boyd & Vandenberghe 2004).

As shown in Section 3.3, least squares without regularization often produces rough and unrealistic solutions even with noise-free data. This is because the slip model is typically overparametrized, such that the data can be fit well with a variety of models, many of which contain rapid spatial or temporal oscillations between positive and negative slip. Regularization can be used to avoid these physically implausible models, and we experiment with both damping and smoothing, as described in the following.

2.3.2 Damped least squares

When the prior model has a complex Gaussian distribution, $\mathcal{C}N(\mathbf{m}_0, \sigma_m^2\mathbf{I})$, the posterior PDF (3) also obeys a Gaussian distribution:

$$\begin{aligned}p(\mathbf{m}|\mathbf{d}^0) = c_0 \exp\Bigg(&-\frac{1}{\sigma^2}[(\mathbf{d}^o - \mathbf{G}\mathbf{m})^{\mathrm{H}}(\mathbf{d}^0 - \mathbf{G}\mathbf{m}) \\ &+ \frac{\sigma^2}{\sigma_m^2}(\mathbf{m} - \mathbf{m}_0)^{\mathrm{H}}(\mathbf{m} - \mathbf{m}_0)]\Bigg),\end{aligned} \tag{7}$$

where $\mathbf{m}_0$ is the prior model, which can integrate already existing information of the slip-rate into the inversion. When $\mathbf{m}_0 = \mathbf{0}$, the MAP is given by

$$\hat{\mathbf{m}} = \arg\min_{\mathbf{m}} \|\mathbf{d}^o - \mathbf{G}\mathbf{m}\|_2^2 + \alpha^2\|\mathbf{m}\|_2^2, \tag{8}$$

where

$$\alpha^2 = \frac{\sigma^2}{\sigma_m^2} \tag{9}$$

is the variance ratio of $\mathbf{n}$ and the prior model. It is challenging to find the best value for α^2 without information about σ_m^2. Large α^2 enforces the model to be close to the prior model $\mathbf{m}_0 = \mathbf{0}$. Small α^2 is preferred because it puts more weight on the data. The model maximizing eq. (7) is the damped least-squares solution of this QP problem and attempts to find the lowest spectral power consistent with the data. The degree of damping controlled by the adjustable parameter α^2.

2.3.3 Spatial smoothing

When the complex-valued slip-rate is assumed to be spatially smooth, the prior model can be expressed as:

$$p(\mathbf{m}) = c_0 \exp\left(-\frac{1}{\sigma_l^2}\mathbf{m}^{\mathrm{H}}\mathbf{L}^{\mathrm{H}}\mathbf{L}\mathbf{m}\right), \tag{10}$$

where $\mathbf{L}$ is the Laplacian matrix (Claerbout & Fomel 2008), a 2-D discrete second order finite difference operator and $\sigma_l^2/(\mathbf{L}^{\mathrm{H}}\mathbf{L})$ is the covariance matrix. Other smoothing matrices, such as the Gaussian smoothing matrix could also be used. Note that the operator applies to both the magnitude and phase of the spectra of connecting subfaults. The estimation under this assumption has spatial smoothing:

$$\hat{\mathbf{m}} = \arg\min_{\mathbf{m}} \|\mathbf{d}^o - \mathbf{G}\mathbf{m}\|_2^2 + \lambda^2\|\mathbf{L}\mathbf{m}\|_2^2, \tag{11}$$

where the degree of smoothing is controlled by the adjustable parameter

$$\lambda^2 = \frac{\sigma^2}{\sigma_l^2}. \tag{12}$$

As in the damped least-squares approach, this is also a QP problem.

2.3.4 Compressive sensing

If slip is known to be spatially rough, it may be more appropriate to assume a prior that encourages spatially sparse solutions, such as a Laplacian distribution:

$$p(\mathbf{m}) = c_0 \exp\left(-\frac{1}{b}\sum_i^M |m_i - \mu_i|\right), \tag{13}$$

where $\boldsymbol{\mu}$ is the model mean, and b is a scale parameter. The MAP solution encourages sparsity and is termed compressive sensing (e.g. Yao *et al.* 2011; Xenaki *et al.* 2014), when $\boldsymbol{\mu} = \mathbf{0}$:

$$\hat{\mathbf{m}} = \arg\min_{\mathbf{m}} \|\mathbf{d}^0 - \mathbf{G}\mathbf{m}\|_2 + \beta^2\|\mathbf{m}\|_1. \tag{14}$$

This is a second-order cone problem (SOCP), and can be efficiently solved with convex optimization (Boyd & Vandenberghe 2004). Similar to smoothing, the degree of roughness is controlled by the adjustable parameter β^2.

2.3.5 Combined constraints

In general, optimal inversion strategies may involve a combination of the constraints listed above and we have experimented with this approach for the SIV1 problem. For example, the model can be required to be damped, spatially smooth, and with fixed boundary patches:

$$\begin{aligned}&\hat{\mathbf{m}} = \arg\min \|\mathbf{d}^o - \mathbf{G}\mathbf{m}\|_2^2 + \lambda^2\|\mathbf{L}\mathbf{m}\|_2^2 + \alpha^2\|\mathbf{m}\|_2^2 \\ &\text{s.t.} : \mathbf{W}_0\mathbf{m} = \mathbf{0},\end{aligned} \tag{15}$$

where $\mathbf{W}_0$ is a selecting matrix, where elements corresponding to boundary patches are 1 and the rest are zero. Both the objective

function and constraint are convex (Boyd & Vandenberghe 2004), which assures a unique solution for the inverse problem.

The problem is greatly stabilized with the regularization strategy described in eq. (15). Fixing the fault boundary patches to zero while asking the slip-rate to be spatially smooth enforces the slip-rate to gradually decrease to zero at boundaries. This makes physical sense and will not introduce errors, since the modelled fault plane is overparametrized and we can make it larger than the ruptured area.

2.4 Negative slip

Eq. (15) is in the frequency domain, thus to obtain the time-domain slip function, $\mathbf{m}$ must be Fourier transformed. The method assumes the signal $\mathbf{d}^o$ recorded by the seismic stations is accurately given by the computed Green's functions, that is that there is coherent signal in the frequency-domain to be modelled. However, there are no assumptions of coherence across frequency or time. The slip at each frequency sample is independent and time slip functions are obtained via the inverse Fourier transform. This is in contrast to other slip-inversion schemes where time slip is often assumed to consist of one or more basis rise-time functions. The advantage of basis rise-time functions is that the number of unknowns can be greatly reduced, that is typically only a few unknowns are needed per cell (e.g. starting and ending times, amplitude, and a few more to define the function shape). However, this limited parametrization may prevent resolving some of the complexities of real earthquake ruptures, such as multiple slip events on the same subfault. In contrast, eq. (15) has one complex-valued unknown per cell per frequency (for the SIV1 inversion, $2 \times 50 = 100$ parameters are used per cell), giving considerably more freedom in obtaining the true slip function.

Negative slip is physically unrealistic and can be eliminated by limiting the search space to only contain positive amplitudes as is often done for global search methods (e.g. Ji *et al.* 2002) or in classical least squares by using a positivity constraint (e.g. Yagi 2004). However, implementing a non-negative slip constraint is difficult in frequency-domain methods and we do not impose such a constraint, but the regularization tends to reduce negative slip. Instead, we use the size of the negative slip patches as a measure of the quality of the inverse solution. Well-resolved models should have only small amounts of negative slip and the positive slip patches have uncertainties similar to the magnitude of the negative slip. Note, however, that the absence of significant negative slip does not guarantee an accurate model, as we will show in Section 3.3.

2.5 Misfit measure

The inversion is performed in the frequency domain and includes regularization, see eq. (15). To quantitatively investigate inverted solutions, we compute the time-domain misfit parameter for the ith station:

$$\epsilon_i = \sum_{j=x,y,z} \|\mathbf{d}^o_{i,j}(t) - \hat{\mathbf{d}}_{i,j}(t)\|_2^2, \tag{16}$$

where $\mathbf{d}^o_{i,j}(t)$ is the jth component at the ith station; $\hat{\mathbf{d}}_{i,j}(t) = \mathcal{F}^{-1}[\mathbf{G}\hat{\mathbf{m}}(f)]_{i,j}$ is the jth component synthetic seismogram at the ith station from the inverted rupture model. The misfit reduction is defined as

$$\text{Misfit reduction} = 1 - \sqrt{\frac{E}{E_0}}, \tag{17}$$

where $E = \sum_{i=1}^{N} \epsilon_i$ is the total misfit and we have normalized with the norm of the data $E_0 = \sum_{i=1}^{N} \sum_{j=x,y,z} \|\mathbf{d}^o_{i,j}(t)\|_2^2$. When noise is present in the recordings, the signal-to-noise ratio (SNR) is defined as signal power over noise power

$$\text{SNR} = \frac{\sum_i^N \sum_{j=x,y,z} \|\mathbf{d}^o_{i,j}(t)\|_2^2}{\sum_i^N \sum_{j=x,y,z} \|\mathbf{n}_{i,j}(t)\|_2^2}, \tag{18}$$

where $\mathbf{n}_{i,j}(t)$ is the noise added to the corresponding recording $\mathbf{d}^o_{i,j}(t)$. In addition to SNR, we construct a normalized noise parameter similar to misfit as

$$\text{Noise level} = \left(\frac{\sum_i^N \sum_{j=x,y,z} \|\mathbf{n}_{i,j}(t)\|_2^2}{\sum_i^N \sum_{j=x,y,z} \|\mathbf{n}_{i,j}(t) + \mathbf{d}^o_{i,j}(t)\|_2^2} \right)^{1/2}. \tag{19}$$

3 SYNTHETIC TESTS

3.1 Problem description

Exercise 1 of the SIV (http://equake-rc.info/) is used as a synthetic test case (Mai *et al.* 2007; Page *et al.* 2011; Mai 2013). Right-lateral strike-slip motion occurs on a fault with dip 80° and strike 90° (see Fig. 1). The rupture remains buried and does not reach the surface. The fault plane is 36 km in length and 18 km in downdip extent with top and bottom depths of 2.046 and 19.772 km. The seismic moment M_0 is 1.06×10^{19} Nm (M_w 6.62). The hypocentre location is (9.2, 2.5 and 14 km) in a right-lateral Cartesian system. The earthquake source model and its corresponding synthetic seismograms are generated using a spontaneous dynamic rupture model with heterogeneous initial stress on the fault. While the initial normal stress varies simply with depth, initial shear-stress is parametrized in terms of a von-Karman autocorrelation function (these and other details of the rupture simulation provided by Martin Mai, personal communication, 2014). The dynamic modelling assumes a linear slip-weakening friction law, with static and dynamic friction of 0.6 and 0.55, respectively. The dynamic rupture modelling is performed with a 3-D generalized finite-difference method (Ely *et al.* 2008, 2009), with 100 m spatial discretization and 0.008 s time increments. The resulting slip-rate functions on the fault show Kostrov-type behaviour with local variations due to the heterogeneous initial shear-stress. The peak final slip on the fault is smooth with an elliptical shape in the along-strike direction (Fig. 1a). Rupture propagation over the fault is fairly smooth, with small variations due to the stress variability (Fig. 1b), while the rise time distribution within the rupturing area is quite heterogeneous. Rupture speed averages about 2.8 km s^{-1}, but varies over the fault, which causes the rupture time, slip and slip-rate to be somewhat heterogeneous. Total rupture duration is less than 10 s. This assumed rupture model will be the focus of our inversion efforts and will henceforth be termed the SIV1 model. To compute synthetic seismograms, a layered velocity structure and station geometry is assumed (Figs 2 and 3). There are a total of 40 three-component receivers, providing 120 recordings that can be used for inversion. Stations are well-distributed on the surface around the fault. Both the SIV1 model and synthetics are provided as part of the SIV exercise.

We first regenerate the observed data using the provided velocity structure and source–time functions using the COMPSYN program (Spudich & Archuleta 1987). Our forward synthetics are similar to those provided in the SIV1 exercise for frequencies below 1 Hz (misfit reduction 93.4 per cent, SNR = 229.5). The differences are

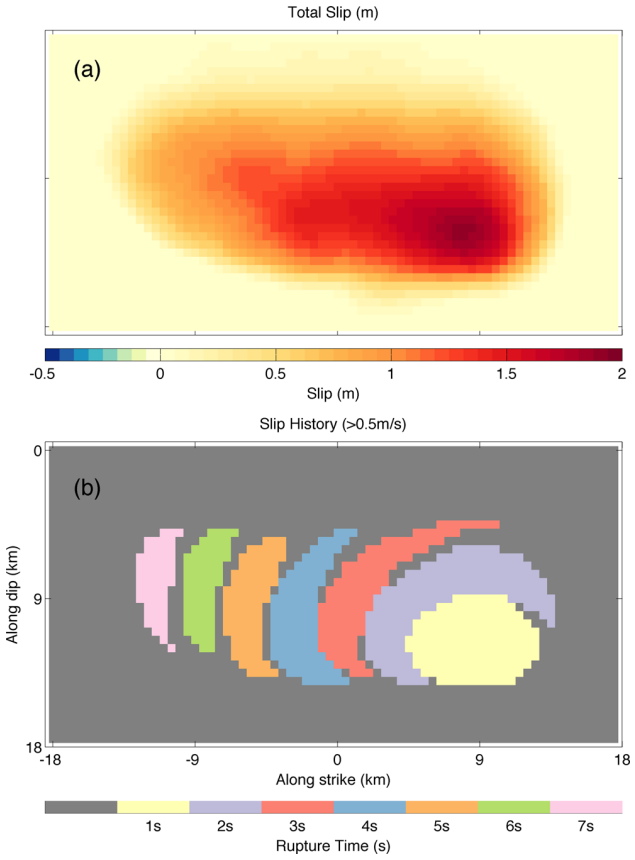

Figure 1. The filtered SIV1 model, (a) integrated total slip; (b) time evolution of slip. For a specific time, only slip-rate functions of the subfaults that are greater than 0.5 m s^{-1}. are plotted in colours other than grey. Parts of the grey area do rupture, but the maximum value of the slip-rate functions do not exceed 0.5 m s^{-1}. The coloured area provides a measure of the rupture front. Because this filtered SIV1 has a wider slip-rate pulse, there are overlapping areas over the fault plane at different times. To better show the rupture progress, the older rupture areas are plotted on top of the newer rupture areas to emphasize the new ruptured areas.

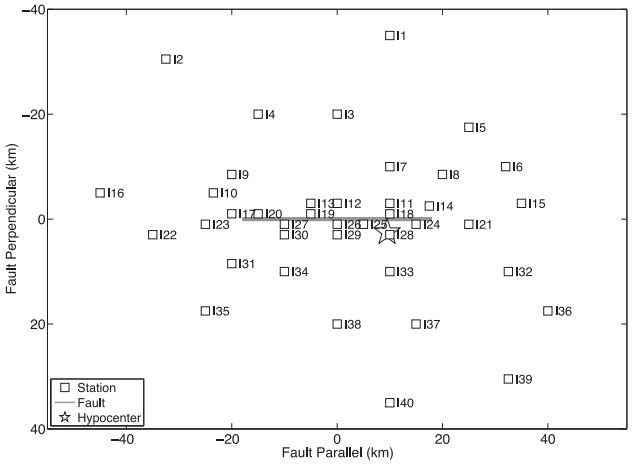

Figure 2. The SIV1 model station distribution. There are 40 three-component stations, providing 120 total records.The rupture remains buried and does not reach the surface. Hypocentre location is (9.2, 2.5, 14) km in this (x, y, z) coordinate system.

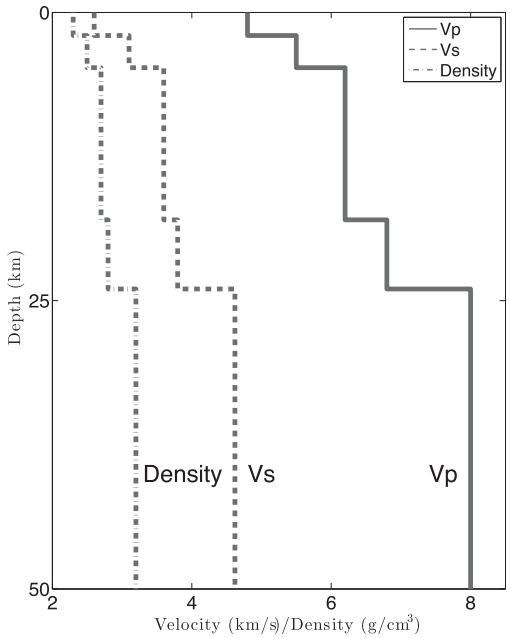

Figure 3. Velocity (km s^{-1}) and density (g cm^{-3}) profile for SIV1. A layered isotropic velocity–density structure is provided for the synthetic test. Q_s and Q_p are assumed to be infinite.

likely related to model assumptions and parameter differences between the SIV dynamic model and COMPSYN. Validating synthetic seismograms is an important part of the SIV process, but is not our focus. To examine the performance of the inversion alone, we use our own forward synthetics, and use SIV1 provided data as a sensitivity test. We restrict our analysis of the seismograms to 1 Hz and below, because real slip inversion typically avoid data above 1 Hz where scattering and other effects reduce waveform coherence (Cormier 2007).

3.2 Inversion strategies

Assuming that the fault-plane geometry and slip rake are specified, the model unknowns are just $\mathbf{m}^s$ in eq. (2). The fault plane is the same as the true solution, 36 km in length and 18 km in downdip extent. There are $M = 72 \times 36 = 2592$, 0.5 km $\times$ 0.5 km patches used to generate the observed data. We Fourier transform the first 35 s of observed data into the frequency domain to construct $\mathbf{d}^o(f)$, including all wave types (i.e. P waves, S waves, multiples and surface waves). For all the station-patch pairs, Green's functions up to 1 Hz are computed to obtain $\mathbf{G}$. At each frequency, we invert for the spatial distribution of slip-rate via eq. (2). The slip-rate spectra at each point on the fault are then inverse Fourier transformed into the time domain. For the inverse problem, the subfault size is set to be 1 km $\times$ 1 km, which reduces the spatial unknowns to $36 \times 18 = 648$ for each frequency. When the zero-slip boundary constraint is applied, as in eq. (15), the spatial unknowns are $34 \times 16 = 544$ for each frequency.

For all the station-patch pairs, we compute Green's functions to 1 Hz to obtain $\mathbf{G}$ ($\delta f = 0.024$ Hz, 50 frequency bins are used). At each frequency, we then use convex optimization (Boyd & Vandenberghe 2004) to invert for the spatial distribution of slip-rate via eq. (2) or the equivalent regularized version using the CVX package (Grant

Table 1. Regularization parameters and misfit reduction.

Class	α^2	λ^2	Misfit reduction (per cent)[a]	Seismic moment M_0 (Nm)
Least squares			99.2	1.11×10^{19}
Preferred DLS[a]	9.0×10^{-10}		99.2	1.1×10^{19}
DLS1	2.1×10^{-5}		97.0	8.8×10^{18}
DLS2	2.3×10^{-3}		65.7	8.0×10^{17}
DLS3	6.7×10^{-3}		47.9	2.8×10^{17}
Preferred SS[a]		4.0×10^{-8}	99.2	1.1×10^{19}
SS1		3.6×10^{-5}	97.8	1.3×10^{19}
SS2		1.5×10^{-2}	66.9	9.7×10^{18}
SS3		5.1×10^{-2}	47.9	9.5×10^{18}
Preferred regularization[a] (2 km by 2 km)	9.0×10^{-10}	4.0×10^{-8}	99.1	1.2×10^{19}
Preferred regularization (1 km by 1 km)	9.0×10^{-10}	4.0×10^{-8}	99.2	1.1×10^{19}
Preferred regularization (0.5 km by 0.5 km)	9.0×10^{-10}	4.0×10^{-8}	99.2	1.1×10^{19}
SIV1 DLS1	2.1×10^{-5}		95.9	9.1×10^{18}
SIV1 DLS2	2.3×10^{-3}		66.2	8.3×10^{17}
SIV1 DLS3	6.7×10^{-3}		48.7	3.0×10^{17}
SIV1 SS1		3.6×10^{-5}	96.4	1.4×10^{19}
SIV1 SS2		1.5×10^{-2}	65.0	1.0×10^{19}
SIV1 SS3		5.1×10^{-2}	46.1	9.9×10^{18}
SIV1 provided data	2.3×10^{-8}	1.0×10^{-6}	93.1	1.2×10^{19}
1 per cent Gaussian noise	9.0×10^{-9}	4.0×10^{-7}	81.8	1.1×10^{19}
10 per cent Gaussian noise	9.0×10^{-7}	4.0×10^{-5}	12.6	8.6×10^{18}
70° dip[1]	9.0×10^{-10}	4.0×10^{-8}	88.7	9.0×10^{18}
70° dip[2]	2.6×10^{-8}	1.0×10^{-4}	75.9	9.4×10^{18}
90° dip[1]	9.0×10^{-10}	4.0×10^{-8}	75.1	1.1×10^{19}
90° dip[2]	1.0×10^{-7}	1.0×10^{-4}	71.1	1.0×10^{19}
170° rake[1]	9.0×10^{-10}	4.0×10^{-8}	94.8	1.0×10^{19}
170° rake[2]	4.0×10^{-8}	4.0×10^{-6}	92.7	1.0×10^{19}
190° rake[1]	9.0×10^{-10}	4.0×10^{-8}	94.0	1.0×10^{19}
190° rake[2]	4.0×10^{-8}	4.0×10^{-6}	91.8	1.0×10^{19}

[a]DLS represents damped least squares (eq. 8); SS represents spatial smoothing (eq. 11); Preferred regularization (eq. 15). Misfit reduction is calculated by eq. (17). 70° dip[1, 2] represents Figs 19(b) and (c); 90° dip[1, 2] represents Figs 19(d) and (e). 170° rake[1, 2] represents Figs 20(a)–(d); 190° rake[1, 2] represents Figs 19(e)–(h).

& Boyd 2008, 2013). The slip-rate spectra at each point on the fault are then inverse Fourier transformed into the time domain.

Our applied regularization, regularization strength and obtained misfits are summarized in Table 1. Regularization here is used to describe the inversion strategies, such as eqs (8) and (15). Regularization strength refers to eqs (9) and (12). Retrieved seismic moments (M_0) for each case are also listed in the table.

3.3 No regularization

Fig. 4 shows results of a simple least-squares inversion without regularization. The recovered slip model is much rougher than the SIV1 model (compare Figs 1 and 4) and contains sharp changes in slip amplitude at the smallest spatial scales of the model. The slip-rate function near the hypocentre has a negative-slip precursor and oscillatory ringing for many seconds after slip has ceased in the starting model. The frequency domain fit to the slip-rate function is also poor, with substantially higher power at 0.3–0.8 Hz than contained in the SIV1 model. Note however that the negative slip component of this model is relatively small, just 0.53 per cent of the moment of the positive slip component, Thus, the absence of substantial negative slip in our inversions does not necessarily imply a high-quality inverted rupture model.

The SIV1 slip-rate functions contain substantial energy above 1 Hz, which cannot be recovered from analysis of seismic data below 1 Hz. Thus, we apply a 1-Hz low-pass cosine filter with passband and stopband 0.5 and 1.2 Hz to the SIV1 slip-rate functions. The filtered SIV1 has seismic moment M_0 of 1.05×10^{19} Nm (M_w 6.61). This has little effect on fault maps of total slip (e.g. Fig. 1), but significantly broadens the slip-rate pulses, as shown in Fig. 4(b). We will henceforth refer to this 1-Hz low-pass model as the filtered SIV1 model.

More physically realistic models can be obtained by applying regularization. It is important, however, to realize that these models are not required by the data. The model shown in Fig. 4 achieves a nearly perfect fit to all 120 components of the data seismograms. The misfit reduction is 99.2 per cent according to eq. (17) (Table 1). The model is not unique; there are many models that will produce equivalent fits.

3.4 Regularized inversions

Regularization can help stabilize the inverse problem and produce more physically plausible models. There is a trade-off between how well the model fits the data and satisfies the regularization constraints. This trade-off is controlled by the adjustable regularization parameters that assign relative weights to the regularization constraints and the data fit. This is often illustrated using an L-curve of misfit versus regularization norm. For the SIV1 problem, Fig. 5 shows time-domain data misfit reduction (eq. 17) versus model

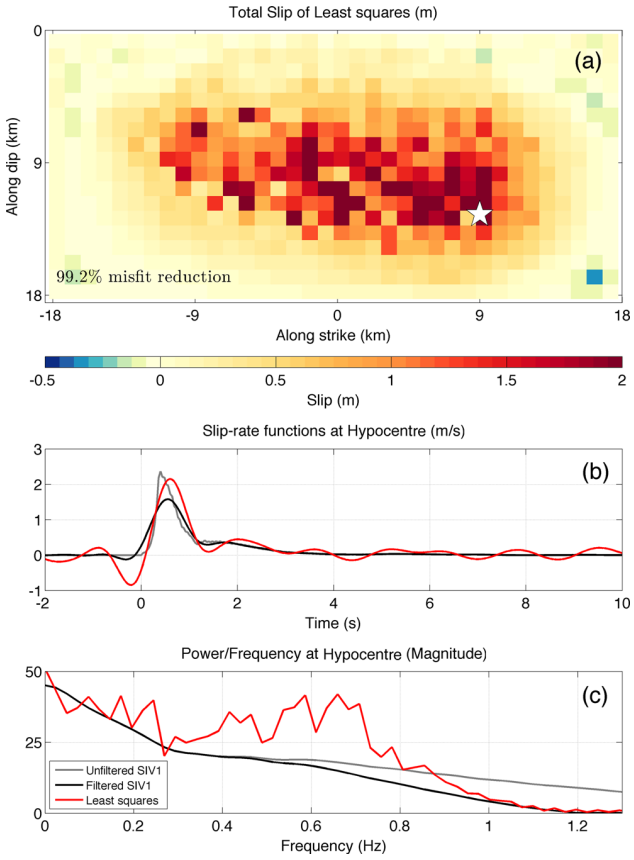

Figure 4. Inverted source model from least squares without any regularizations. (a) Total slip (m), white star indicates hypocentre; (b) Slip-rate function at hypocentre; (c) Power spectrum of the slip-rate function at hypocentre. The misfit reduction of the least-squares model is 99.2 per cent. In (b) and (c), grey lines are from the unfiltered SIV1 model (dynamic simulation); black lines are filtered SIV1 model and red ones are inverted least-squares model.

norm for both damping and smoothness constraints. Increasing the regularization strength produces larger misfit and smaller, smoother models. An example of the fit to a seismogram is plotted in Fig. 5, both in the time and frequency domains. The Y component of Station 23 is used, which has the largest absolute peak. In principle, the regularization parameters should be frequency dependent, since we are performing the inversions independently at each frequency. However, for simplicity we use the same regularization parameters at all frequencies.

Ideally, choosing regularization strength would be informed by the expected level of data misfit, that is to avoid fitting the data better than their noise level. However, data uncertainties can be difficult to quantify, so the process of setting regularization strength can be somewhat subjective. Because our SIV1 synthetics have no noise, we initially apply very weak regularization, enough to provide a more physically realistic solution, but not enough to cause more than a tiny increase in data misfit. For real data sets or synthetic data with errors (Section 5), stronger regularization is required.

The inverted source model with the preferred regularization (eq. 15) is plotted in Fig. 6. It achieves a 99.2 per cent data misfit reduction and a good overall fit to the filtered SIV1 model, both in terms of total slip and slip-rate functions at selected points on the fault (Fig. 6). The total moment of this model is 1.10×10^{19}N · m ($M_w = 6.62$), compared to 1.05×10^{19}N · m ($M_w = 6.61$) for filtered SIV1. Note that these numbers are integrated moments, computed by subtracting the negative slip patches from the positive slip patches. However, the negative slip moment is small compared to the positive slip, just 0.63 per cent of the moment of the positive slip. Synthetic seismograms from the inverted rupture model and previous cases are shown in Fig. 7. Differences with the synthetic seismograms are indistinguishable. These differences between inverted slip models are a clear demonstration of the non-uniqueness of the problem. Even setting the negative slip patches to zero, the resulting model predictions still fit the data reasonably well (91.5 per cent misfit reduction).

This, and other regularized inversions we have tried, locate the correct hypocentre and resolve the rupture velocity and direction, none of which were prescribed. The colours in Fig. 6(b) give the areas that have slip-rates larger than 0.5 km s^{-1} at discrete specified timings, which provides a measure of the rupture front. Because this filtered SIV1 has a wider slip-rate pulse, there are overlapping areas over the fault plane at different times. To better show the rupture progress, the older rupture areas are plotted on top of the newer rupture areas in Fig. 6(b), which emphasizes the new ruptured area. Fig. 8 shows the wavefront snapshots (no time smoothing or averaging) of the original unfiltered SIV1, the filtered SIV1, the least-squares solution, and the inverted source model with our preferred regularization. Smeared rupture fronts are obtained compared to sharp images of SIV1, which is expected given the spatial smoothing regularization. Negative slip patches are scattered over the fault plane in the least-squares solution, see Fig. 8(c). Regularization tends to reduce negative slip rate as seen in Fig. 8(d).

Arrival times of the peak of the slip-rate function with respect to distance from the hypocentre are plotted in Fig. 9. Rupture velocity can be estimated with wavenumber filtering (Olson & Anderson 1988). Here, for simplicity, the slope of the curve is inferred as inverse rupture velocity. Inverted versus model rupture velocities along AA′ are compared in Fig. 9. Spatial changes like the fast rupture velocity near the hypocentre (a result of the assumed 1-km-wide slip initiation zone in the SIV1 model) and a nearly constant rupture velocity on the left fault plane are well resolved. The shaded zone shows the 90 per cent-peak zone of the inverted slip-rate functions. Note that the smoothing constraint introduces some small differences between the inversion result and SIV1, for example the inverted source model has earlier rupture at shallower depth (see 1 s in Fig. 8), earlier initial slip and later peak slip in the slip-rate functions (Fig. 6), causing a timing offset between the preferred model and SIV1 (see Fig. 9).

4 DISCUSSION

These results represent a best-case scenario for rupture inversion from near-field data because they result from a good station distribution, noise-free seismograms, perfectly known Green's functions and exact knowledge of the true fault geometry. We will explore the effect of relaxing some of these advantages in Section 5, but first we consider the resolution limits. The maximum frequency is 1 Hz, which gives a minimum *S*-wavelength of about 3.5 km over the fault. This provides an estimate of the spatial resolution, as evidenced by the smearing of the sharp wavefronts in the starting model into broader features in the recovered model (see Fig. 8). This agrees with Fukahata *et al.* (2014), who explored the resolution limits of slip inversions with good data coverage and exact Green's

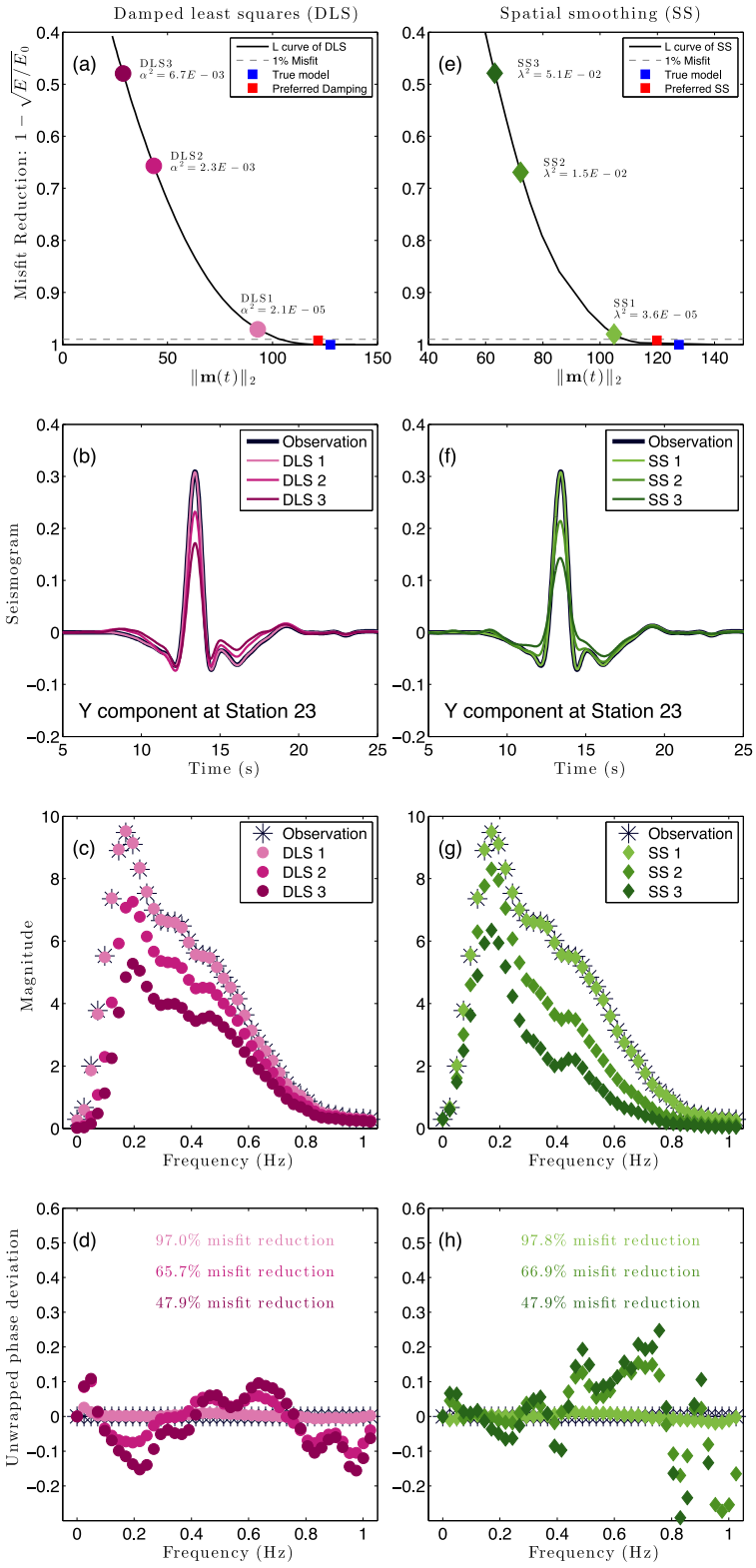

Figure 5. Trade-off ('L') curves of data misfit versus model norm (top row) and example data fits for station 23 in the time domain (second row), the frequency magnitude (third row) and frequency phase (fourth row). The left-hand column shows results of damped least squares, the right-hand column for spatial smoothing. The L curve is computed in the time domain using the entire model and all of the data fits. The Y-component of station 23 is shown because it has the largest peak value of all the recorded data. The three plotted misfit curves correspond to the three labelled points on the L curves. Horizontal dashed lines in (a) and (e) represent 1 per cent misfit level; red square represents the values we used for the preferred regularization; blue square is the model norm [$\|\mathbf{m}(t)\|_2$] and zero misfit of the filtered SIV1 model.

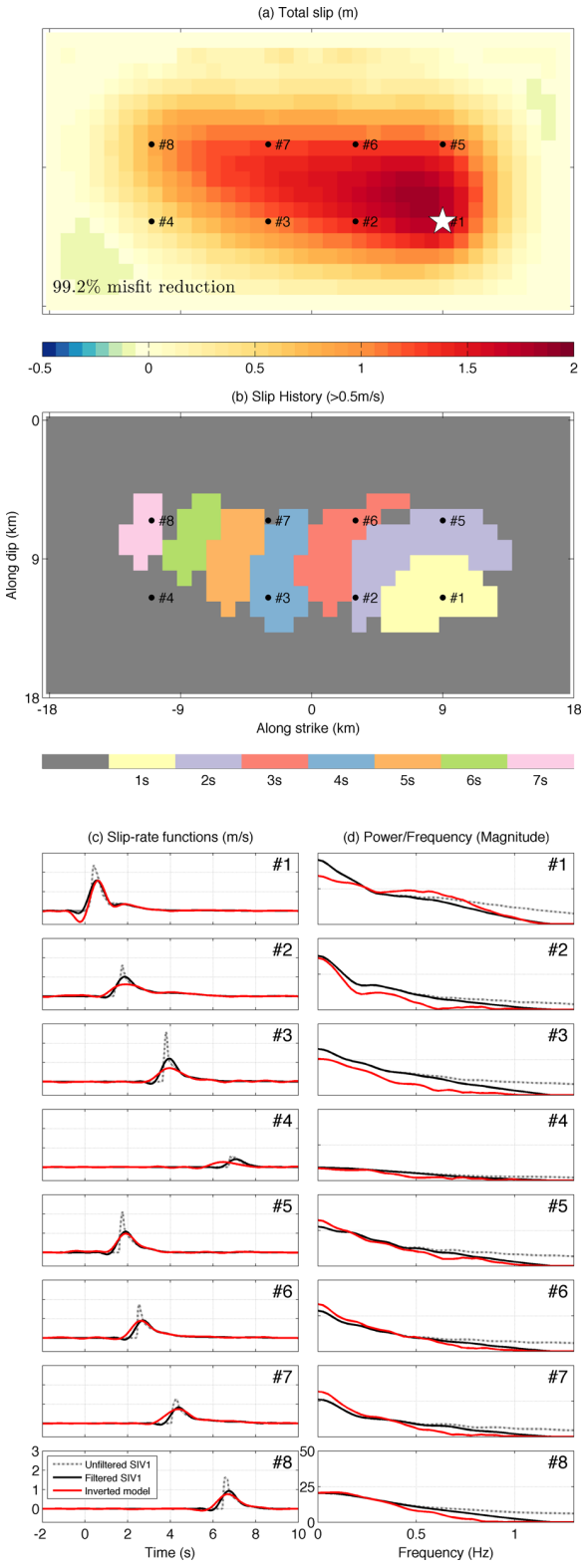

Figure 6. Preferred ruptured model from combined regularization (see text), (a) total slip; (b) slip history; (c) slip-rate functions at given points; (d) power spectrum of the slip-rate functions at given points.

functions. We also experimented with 2 km × 2 km and 0.5 km × 0.5 km model subfault sizes (see Fig. 10, Table 1). A large patch size intrinsically enforces a simple smoothness constraint (0.5 km × 0.5 km patches within each large patch have the same spectrum). Although this model is coarser, it nonetheless achieves a 99.1 per cent misfit reduction. However, it has abrupt changes in slip across the 2-km cell boundaries. The smaller patch size of 0.5 km is more computationally expensive than our 1-km-patch preferred model, but yields little improvement in model resolution or data fit, due to the spatial resolution limit.

Similarly, the temporal resolution is limited by the 1 Hz maximum frequency, as illustrated by a comparison of the original and filtered source–time function (see Fig. 6). For this synthetic example, the spatial and temporal resolution could be improved by including higher frequencies. However, this is difficult for fault inversions of real earthquakes because of incoherence in the high-frequency waveforms and the lack of earth models detailed enough to compute accurate synthetic seismograms above 1 Hz (e.g. Cormier 2007; Ide 2007).

In addition to resolution limits, the inverted models suffer other problems: they have some negative slip, they underpredict maximum slip amplitudes and they perform relatively poorly in the low-slip areas of the fault. The low-pass filtering introduces small sidelobes and some negative slip in the time domain. This negative slip is most visible just before the rupture initiation at each point (see Fig. 6). The magnitude of the inverted spectra at each subfault is smaller than the SIV1 model due to the regularizations. The inversion is able to resolve the source–time function and its spectrum better in the high-slip regions near the hypocentre (#1 to #3 and #5 to #8 of Fig. 6) but poorly images the low-amplitude source–time functions at the rupture boundary (#4 of Fig. 6). The rupture front can only be partially resolved after 6 s and the slip-rate quickly diminishes to zero after 7 s (Fig. 8).

Because the inversion is performed in the frequency domain, constraints on the rupture timing and direction are difficult to apply directly. For example, causality suggests there should be no slip on fault patches at times before the arrival of a *P*-wave radiated from the hypocentre at the origin time. Slip timing is part of the spectrum phase and direct constraints on the phase has not been developed and requires further investigation. Similarly, physical considerations suggest that negative slip is unlikely, but as mentioned in Section 2.4, there is no direct way to implement positivity in our inversion scheme unless we decompose the slip-rate functions into a summation of a group of non-negative functions. This decomposition is intrinsically the same as multi-time-window methods, in which case we lose the flexibilities of the frequency domain approach.

The smoothness regularization worked in large part because the SIV1 model is in fact fairly spatially smooth. Thus, imposing a smoothness constraint helped in recovering the true model, even though rougher models could produce equally good data fits. However, ruptures may not always be spatially smooth. Recent results for several earthquakes have suggested complicated rupture scenarios in which models of multiple discrete subevents may provide a more realistic description of the earthquake than smooth, continuous rupture models (e.g. Koketsu *et al.* 2011; Maercklin *et al.* 2012). In these cases, other regularizations will produce better results, for example compressive sensing (Yao *et al.* 2011), which forces the rupture into a sparse set of subevents. As an example, Fig. 11 shows results for a synthetic model with just two isolated sub faults, with #1 rupturing once and #2 rupturing twice at different times.

Compressive sensing (eq. 14) can precisely locate the rupturing locations and times, showing how a frequency domain method can

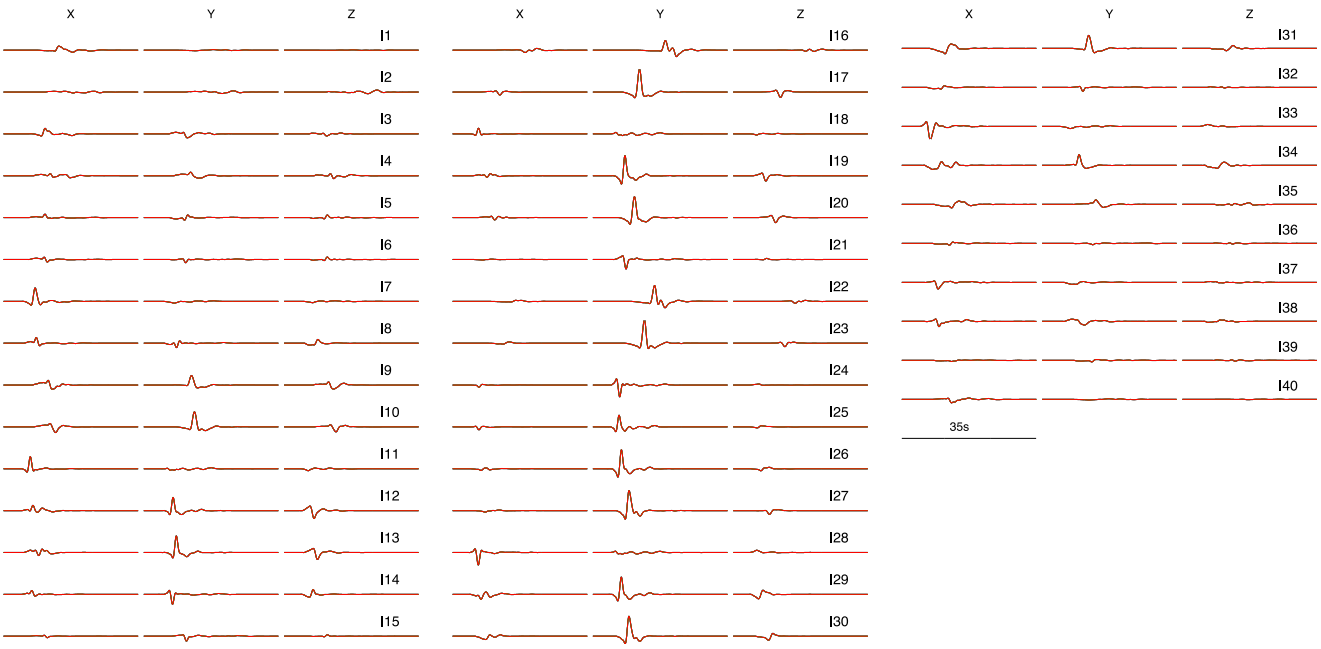

Figure 7. Synthetic seismograms (0–1 Hz) from input and inverted rupture models for least squares, damped least squares, spatial smoothing, preferred regularization combination. The seismograms are indistinguishable.

resolve a complicated multi-subevent earthquake without a well-defined continuous rupture velocity (see Fig. 11a). However, if the same damping and smoothing regularization (eq. 15) is applied as our optimal results for the SIV1 model, the result is an over-damped and smeared version of the true model (see Fig. 11b), which nonetheless fits the data well. In this case, compressive sensing yields effective point sources. However, it cannot resolve the slip versus rupture area trade-off when subfaults are inaccurately parametrized. Thus, no method is guaranteed to be optimal in every case. One advantage in applying a smoothness constraint is that any imaged heterogeneity (e.g. subevents, or multiple slip concentrations) is likely real, as the smoothness regularization attempts to minimize these features.

5 SENSITIVITY TO NOISE OR MODEL ASSUMPTIONS

The inverted source models in Section 3 achieve good spatial and temporal resolution, but are derived from an idealized model with noise-free data, and perfectly known Green's functions. These advantages are not present for inversions of real earthquakes, so it is useful to test how more realistic scenarios affect the resolution. We now explore how the solutions vary with respect to noise and assumed fault geometry.

5.1 Noise and error influence

Noise and errors are inevitable in real slip inversions. Both background microseism noise and signal-generated noise from scattering will contribute to observed seismograms. In addition, Green's functions for the forward problem will never be known perfectly because of unresolved 3-D seismic velocity structure. Thus, it is important to understand the sensitivity of inversion methods to these effects. A method that works for an idealized, noise-free synthetic experiment will be of little practical use if it is overly sensitive to noise and errors. Here we investigate the effects of Gaussian background noise and Green's function or station timing errors. When noise is added into the data, according to eq. (9), the regularization strength should increase to avoid 'overfitting' the data beyond its noise level. The slip-rate magnitude and data fit will decrease as a consequence.

5.1.1 SIV1 provided data

Seismic data provided by SIV1 were generated from the dynamic model described in Section 3.1. As discussed earlier, our computed synthetic seismograms are a close, but not perfect match, to the synthetics provided in SIV1. If we define noise as the difference between our forward synthetics and those from SIV1 (1 Hz low-pass filtered), the misfit reduction is 93.4 per cent. To test the robustness of our approach to small errors in the Green's functions, we performed a source inversion with our preferred regularization, using the filtered SIV1-provided data. The inverted source model is plotted in Fig. 12. The misfit reduction is 93.1 per cent, which is in good agreement with 93.4 per cent as we do not expect to overfit the data. The inverted source model is nearly identical to that of Fig. 6, which is inverted from our synthetic seismograms, and all the key features of the SIV model are recovered, including the slip-rate functions. The total moment of this model is 1.17×10^{19}N $\cdot$ m ($M_w = 6.64$) and the negative/positive slip moment ratio is 0.53 per cent, even less than the 0.63 per cent for the Fig. 6 model. Regularization strength is chosen by an L-curve analysis (see Fig. 13).

A comparison of Fig. 12 to total slip from other SIV EX1 inversion models from the SIV database is shown in Fig. 14. All models used the same data, but the model parametrizations and inversion techniques were different (Gallovič & Zahradník 2012; Razafindrakoto & Mai 2014). We define the misfit as the sum of the absolute differences between the inverted source model and SIV1, normalized by the sum of the total slip of SIV1. Our model yields the

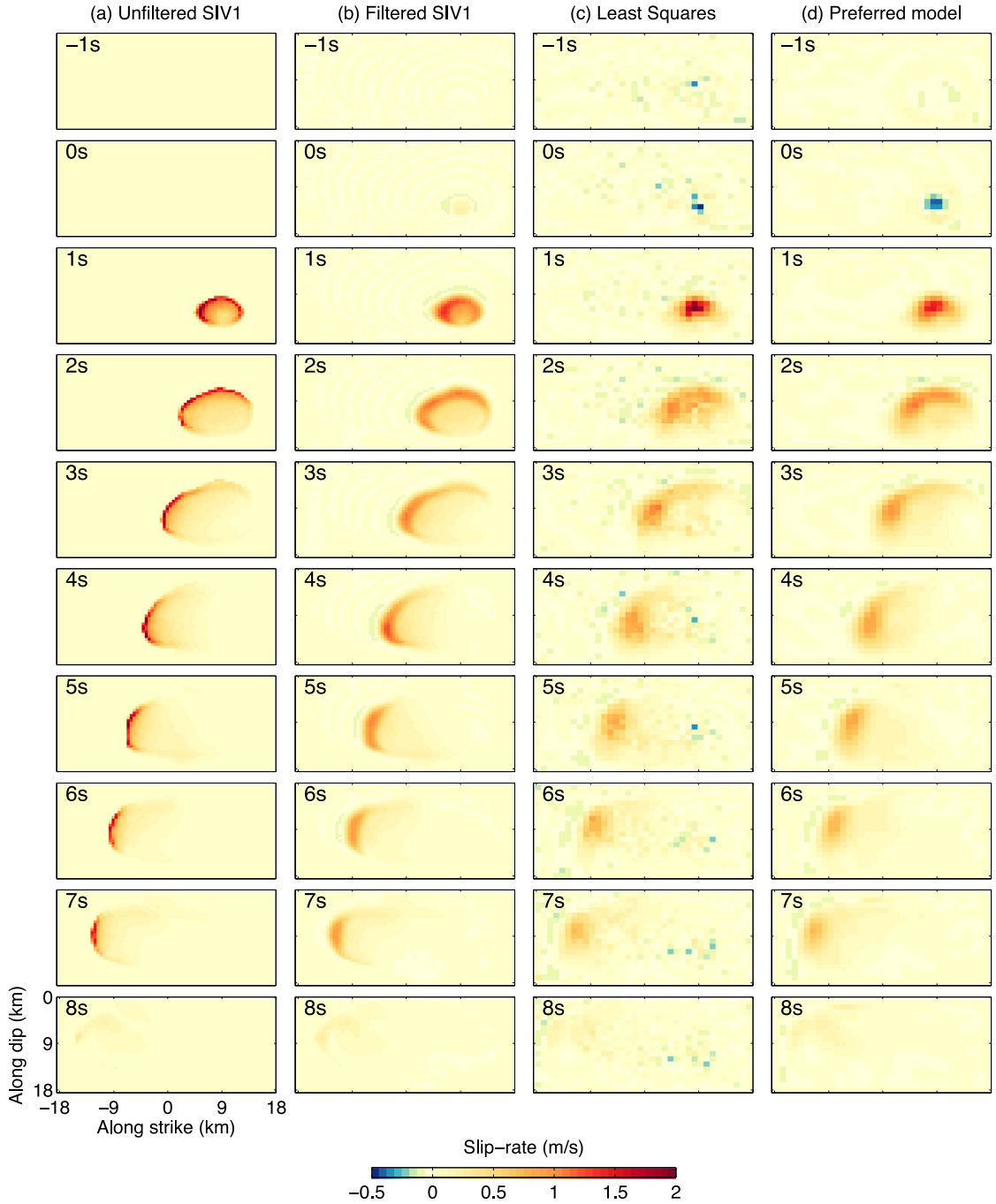

Figure 8. Wavefront snapshots of (a) unfiltered SIV1 model, (b) filtered SIV1 model, (c) least squares (no regularization) and (d) preferred inverted source model with regularization.

smallest misfit, but of course we had the advantage of knowing the true model while optimizing our inversion approach.

5.1.2 Gaussian noise

We simulate both low-noise and high-noise problems by adding to the data white Gaussian noise with zero mean and a standard deviation set to be 1 and 10 per cent, respectively of the peak amplitude of 32 cm s^{-1} of all observed data. Note that 39 per cent (47/120) of the recordings have absolute peak values less than 3.2 cm s^{-1}, so the high-noise model severely affects these records. For the 1 per cent peak amplitude case, $SNR_1 = 2.3$ and $SNR_{10} = 0.023$ for the 10 per cent case.

Inversion results are plotted in Figs 15 and 16. Regularization strength and misfit reduction are shown in Table 1. For the SNR_1 case, we recover the starting model almost as well as the zero-noise case, while achieving a 81.8 per cent misfit reduction (as much as can be expected given the noise level is 18.8 per cent). We found that an increase in regularization strength of 10× was required to achieve this level of misfit.

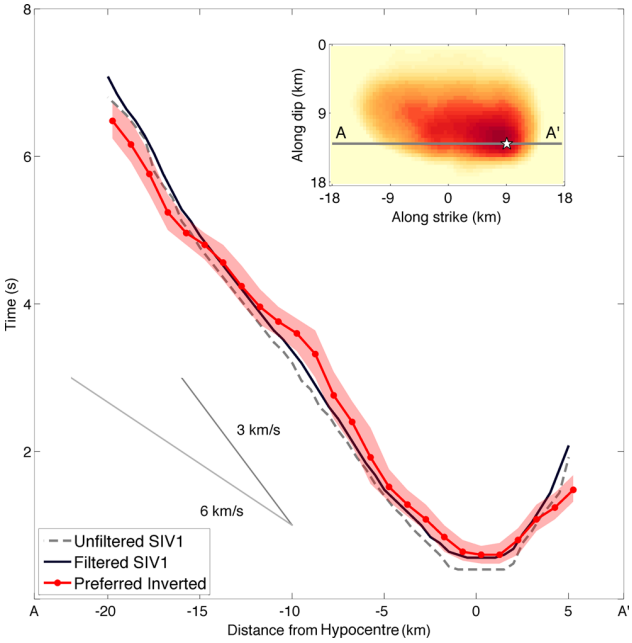

Figure 9. Arrival times of the peak of the slip-rate function with respect to distance from the hypocentre along AA′ on the fault plane. The star shows the zero location of the horizontal axis. Rupture velocity can be inferred from the inverse slope of the time versus distance line. Shaded zone indicate 90 per cent-peak zone of the inverted slip-rate functions.

In contrast, the SNR_{10} noise case introduces considerable error into the inverted source model (see Fig. 16). Following eqs (15) and (12), the strong regularization is 100 times stronger than the SNR_1 case. Although the inverted source model in this case has smeared and small total slip due to the strong regularization (Fig. 16a), the rupture direction and slip history is recovered reasonably well (Fig. 16b). The misfit reduction is 12.6 per cent, which is in good agreement with the noise level, 88.6 per cent. The slip-rate functions are recovered with small oscillations (Figs 16c and d). Synthetic seismograms generated by the inverted source model (Figs 16e–h) fit the noise-free observations data fairly well. Thus the inversion method is robust with respect to even strong Gaussian noise, at least when 40 stations are available to average out its effects.

However, noise may not be Gaussian and it should be recognized that least-squares methods can be severely damaged by non-Gaussian noise (e.g. spikes, clipped data, or other outliers). In these cases, more robust results should be obtainable by using ℓ_1, Huber penalty function or other norms, but we have not yet experimented with these approaches.

5.1.3 Time-shift errors

Another possible source of noise is time-shift errors in the Green's functions caused by unmodelled velocity structure or station timing errors. To simulate this, we randomly time-shift the data, using the same shift for all three components of a station. This time-shift is assumed Gaussian, $\mathcal{N}(0, \sigma_s^2)$. When the standard deviation $\sigma_s \geq 1$, the inversion scheme (eq. 15) fails to recover a reasonable model (see Fig. 17). This is because when the time-shifts are too large, the resulting phase lags in the frequency domain are difficult to resolve. In this case, regularization alone does not work to recover the true model.

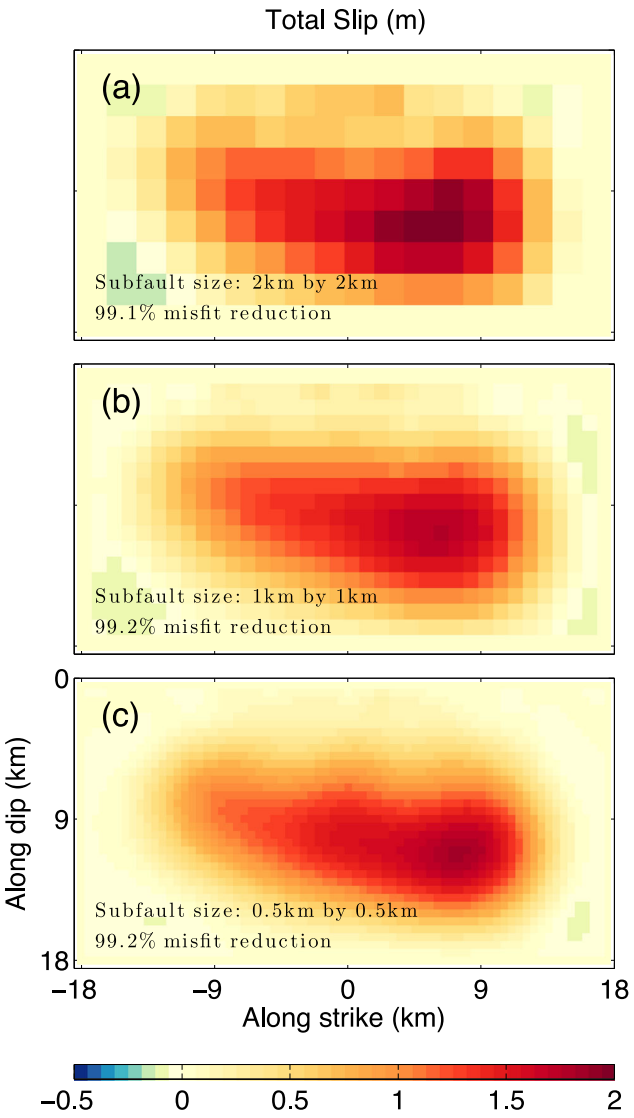

Figure 10. Inverted slip from different subfault sizes. (a) with subfault size as 2 km × 2 km with misfit reduction 99.1 per cent; (b) 1 km × 1 km, as Fig. 6 with misfit reduction 99.2 per cent; (c) 0.5 km × 0.5 km with misfit reduction 99.2 per cent, the finest subfault size as the Green's function calculation.

In real slip inversion problems, static time-shifts are often applied to improve the phase alignment between data and synthetics (e.g. Allmann & Shearer 2007). For our problem with random time-shifts, we find that an iterative approach to estimating these time-shifts is effective. We invert for a starting model from the data assuming all the time-shift terms are zero. We then estimate the time-shift for each station by cross-correlating data and synthetics and apply these empirical time-shifts to the data before inverting again for the slip model. We repeat this until the process converges to a stable slip model and set of time-shifts. For $\sigma_s = 1$, complete convergence is achieved after 15 iterations (see Fig. 18), although the bulk of the model improvement occurs in the first few iterations. Initially, the regularization parameters are set to be $\alpha^2 = 6.4 \times 10^{-6}$ and $\lambda^2 = 4 \times 10^{-8}$, and then set to be the same as the preferred regularization (Fig. 6) during subsequent iterations.

We find that this iterative approach succeeds for our synthetic problem even for quite large σ_s (e.g. $\sigma_s = 5$ s, much longer than most data pulse widths ∼2 s). However, it should be noted that the

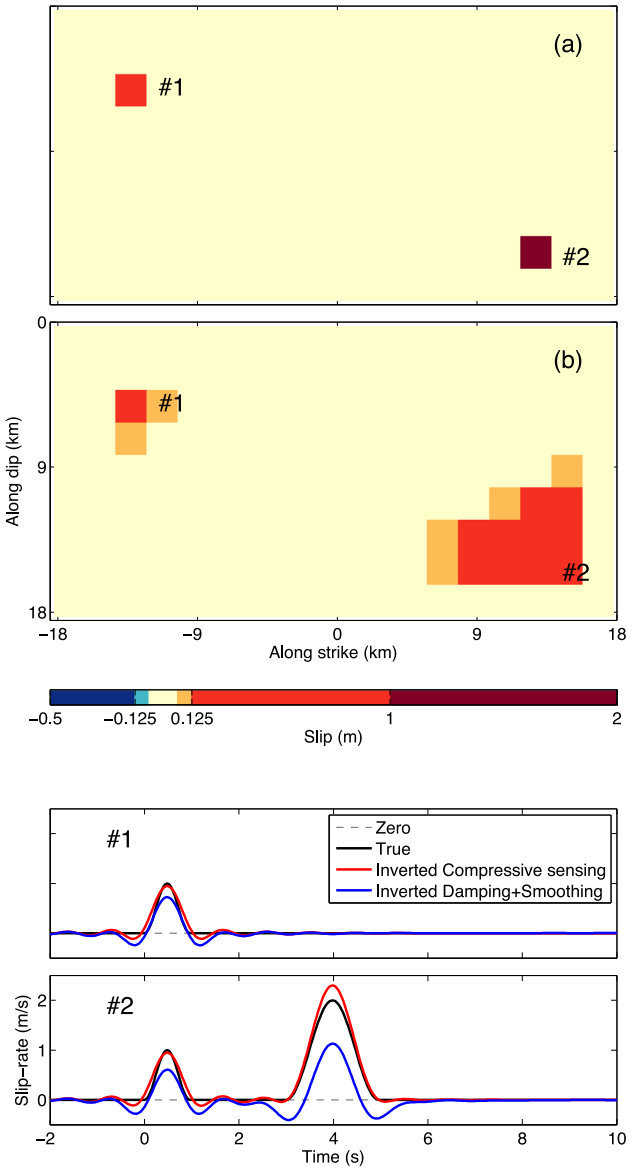

Figure 11. Inverted slip for a sparse rupture model in which only two subfaults ruptured. #1 ruptured once and #2 ruptured twice. The rupture locations and times are well resolved with compressive sensing. Black lines show the true model, red lines are inverted slip-rate functions of compressive sensing and blue lines are inverted slip-rate of damping and smoothing. (a) Inverted slip of compressive sensing, that is eq. (14); (b) Inverted slip with damping and smoothing regularization, that is eq. (15). These models yield data variation reductions of 94.98 per cent for compressive sensing and 94.97 per cent for damping and smoothing. The horizontal dashed line indicates the zero axis.

only source of error is the time-shifts; once these are determined, the slip inversion itself is exactly the same as before. Of course, in reality 3-D velocity structure will distort the shape and amplitude of the Green's functions and may also cause correlated time-shifts among nearby stations rather than the independent random time-shifts assumed here. However, in some cases timing errors may be caused mainly by unmodelled local velocity structure below each station, in which case the shifts may be largely uncorrelated and the iterative empirical approach described here may be effective in recovering a relatively robust rupture image.

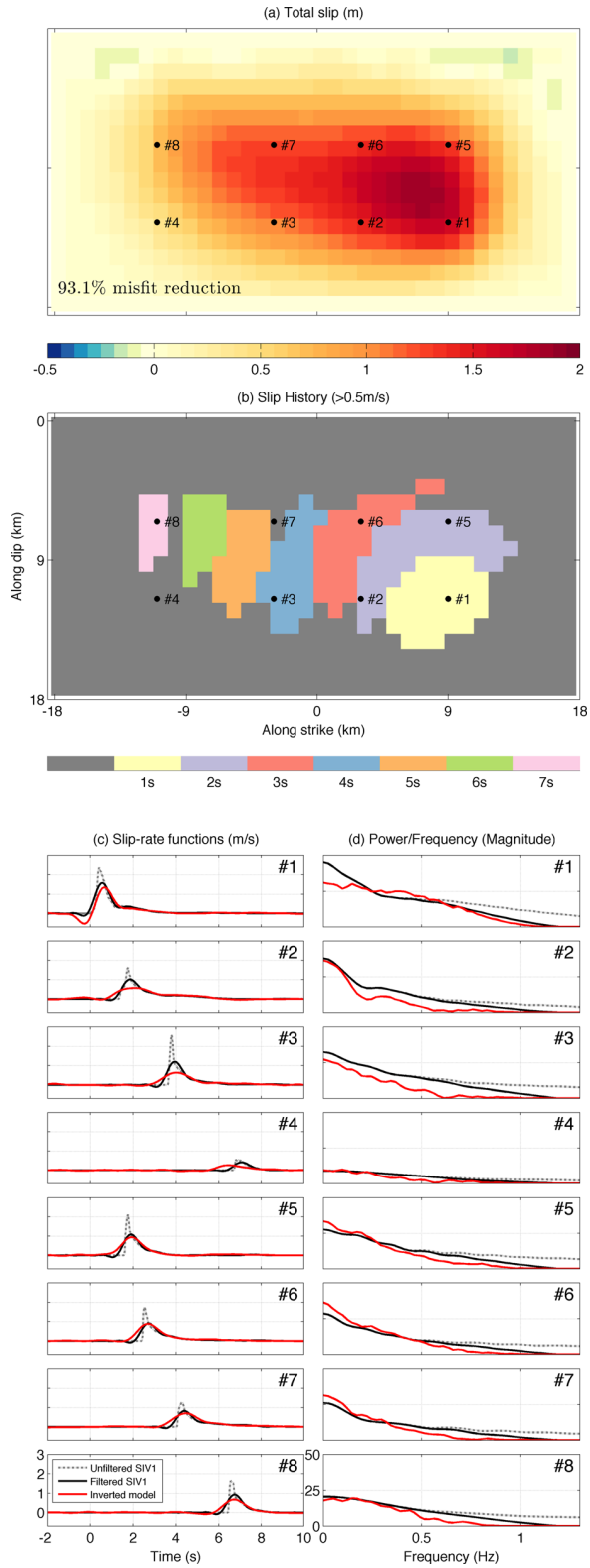

Figure 12. Inverted rupture model by preferred regularization with SIV1 provided data (see text), (a) total slip; (b) slip history; (c) slip-rate functions at given points; (d) power spectrum of the slip-rate functions at given points.

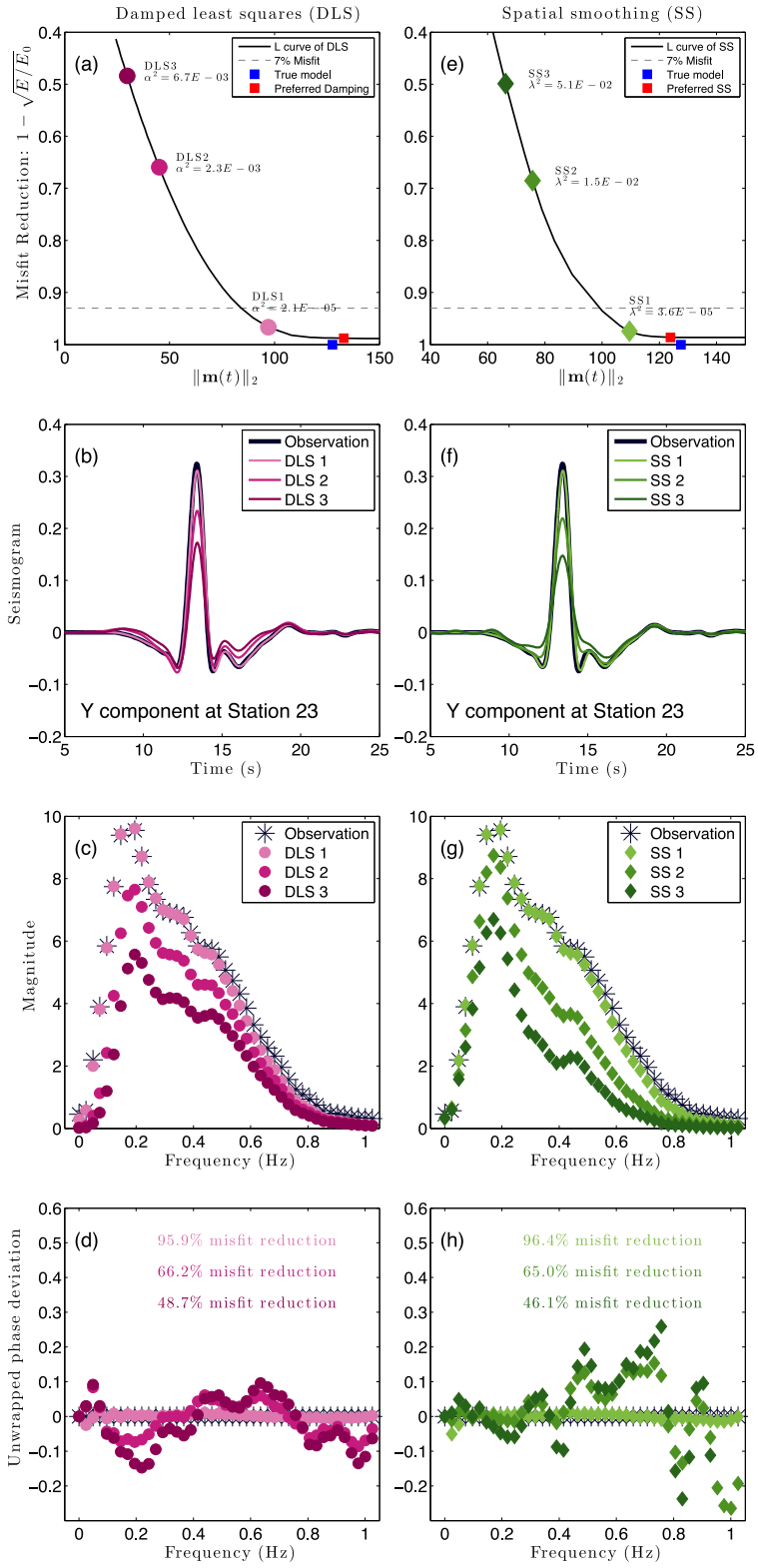

Figure 13. Regularization strength trade-off ('L') curves for inversion with SIV1 provided data (see text). Panel layout is similar to Fig. 5, only the grey dashed line represents 7 per cent misfit level.

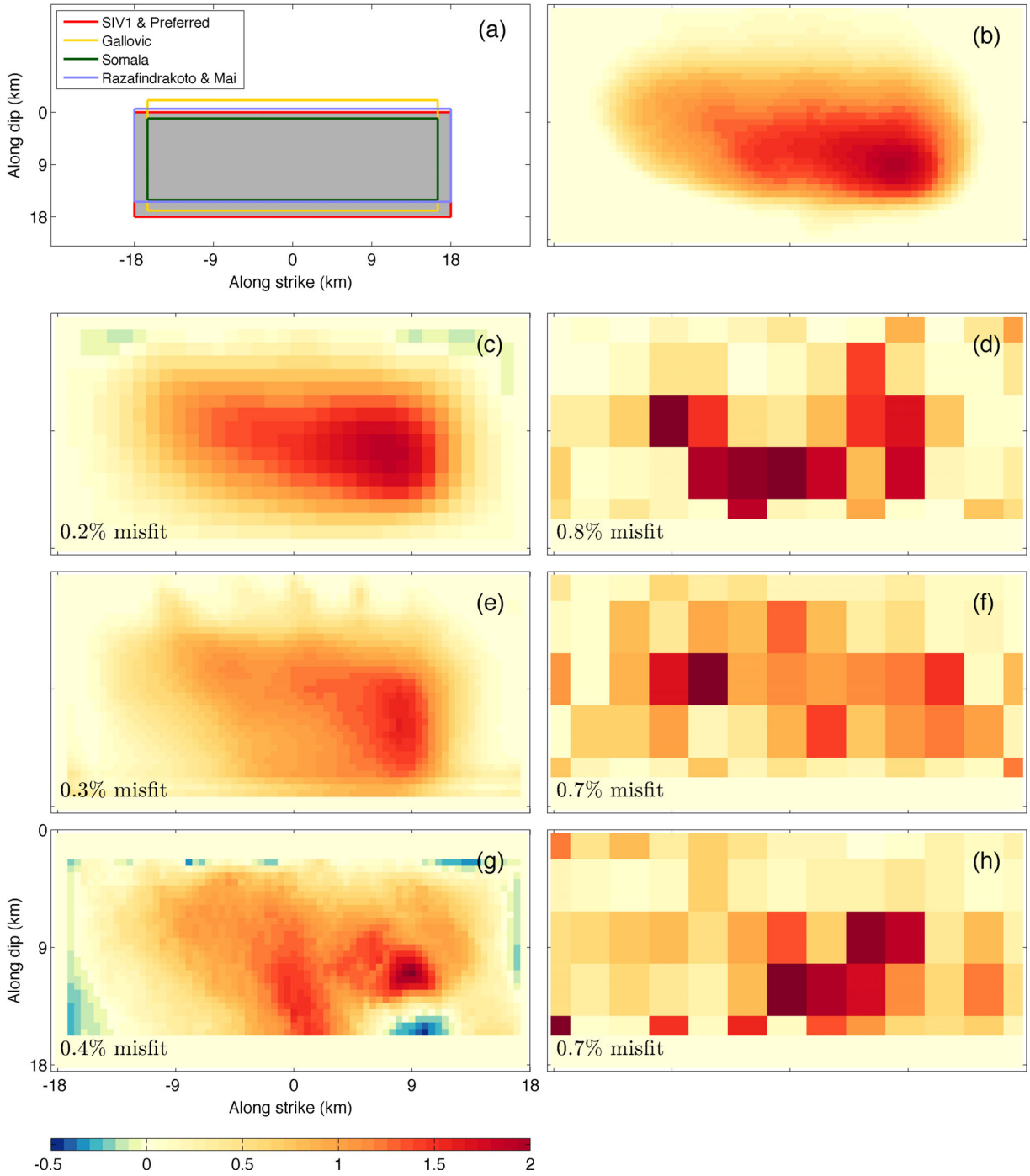

Figure 14. Inverted rupture models by different groups. Misfit is the sum of absolute differences between the inverted model and SIV1 that are normalized by the sum of total slip of SIV1. (a) Parametrization of the fault plane of different groups; (b) filtered SIV1 model; (c) inverted ruptured model by preferred regularization with SIV1 provided data (Fig. 12); (d)–(h) inverted slips by other groups (Gallovič & Zahradník 2012; Razafindrakoto & Mai 2014). (d), (f) and (h) are inverted slips of Razafindrakoto & Mai (2014) using a triangular source–time function, or a Yoffe function with acceleration time Tacc of 0.1 and 0.3 s, respectively.

5.2 Unknown fault geometry

5.2.1 Unknown dip

The inversions so far have used exactly the same fault geometry as the true model. However, the exact position of the fault is often imprecisely known, so it is important to explore the erroneous effects on the slip model of using an inaccurate fault geometry. One of the least well-constrained fault parameters is the fault dip, so this is the parameter we focus on here. We assume the fault surface trace (i.e. position and strike) is the same as the true model, but vary the dip of the assumed fault plane. Deviations of $\pm 10^\circ$ from the true dip of 80° are tested, $\delta_1 = 70^\circ$ and $\delta_2 = 90^\circ$. In each case, we compute

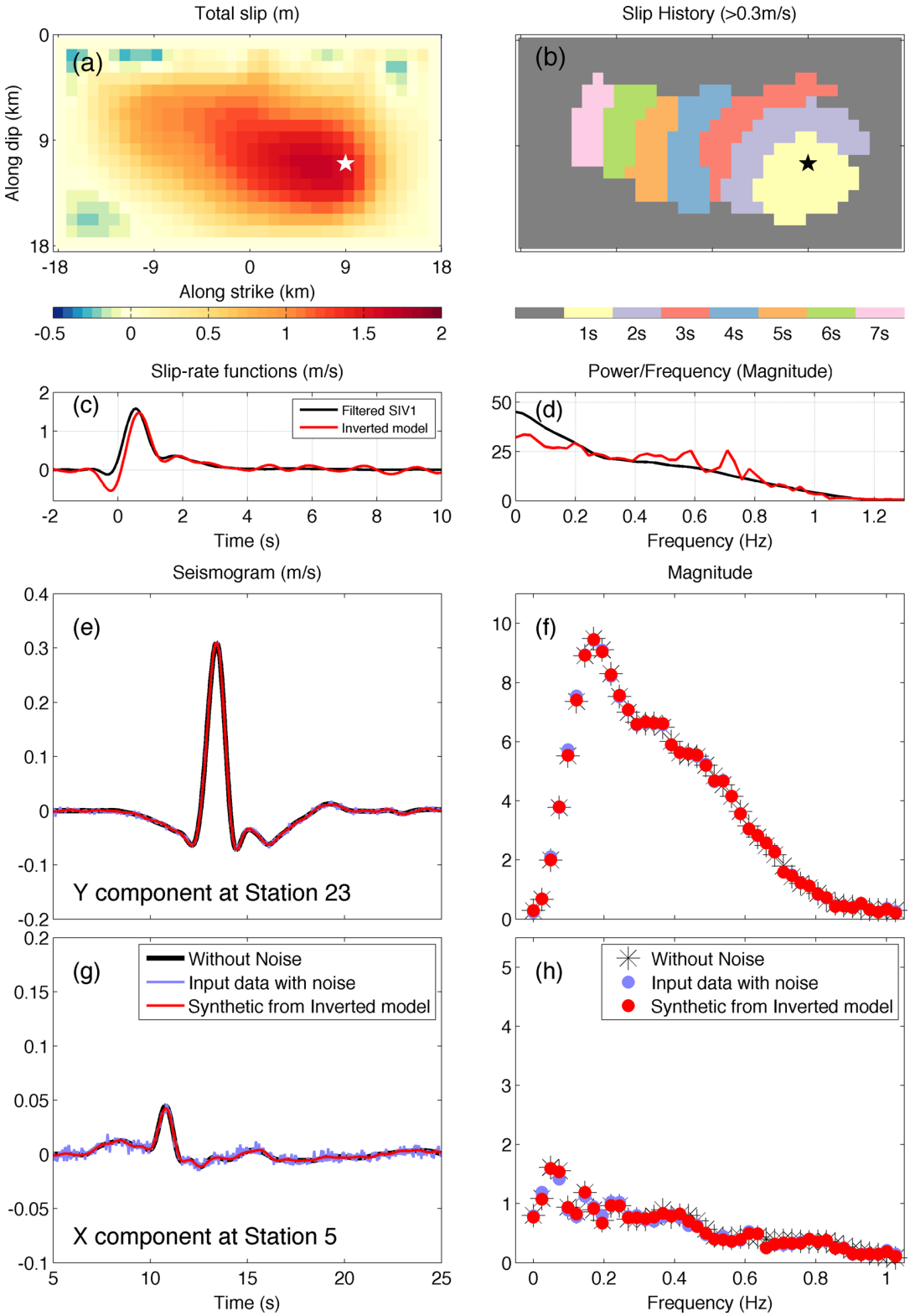

Figure 15. Inverted source model from data with Gaussian noise (SNR_1). (a) Total slip; (b) slip history; (c) slip-rate function at hypocentre; (d) spectrum of the slip-rate function; (e) seismograms with the largest peak amplitude; (f) spectra of the seismograms (e); (g) seismogram with the median peak amplitude; (h) spectra of the seismograms (g).

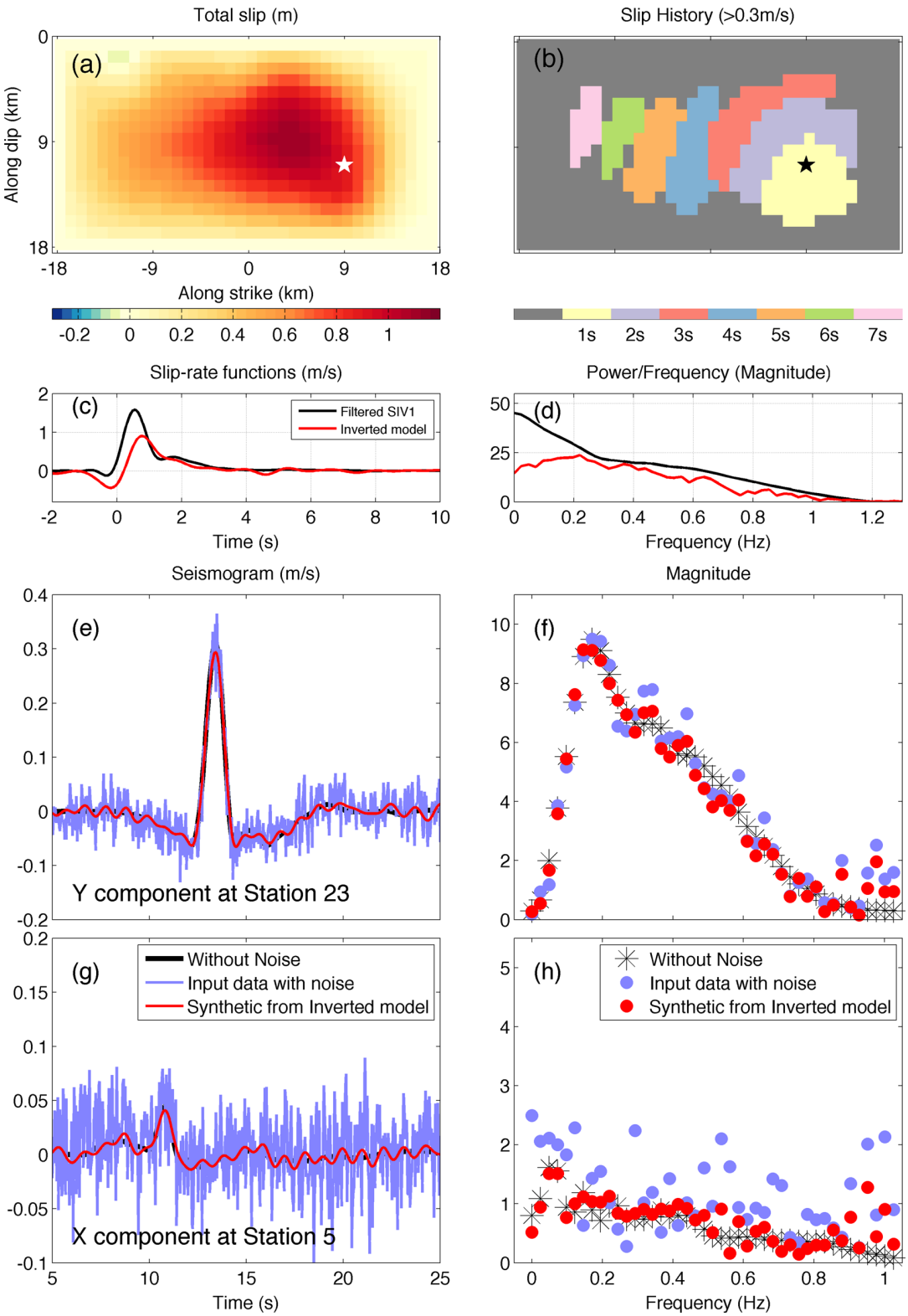

Figure 16. Inverted source model from data with Gaussian noise (SNR_{10}). (a) Total slip; (b) slip history; (c) slip-rate function at hypocentre; (d) spectrum of the slip-rate function; (e) seismograms with the largest peak amplitude; (f) spectra of the seismograms from (e); (g) seismogram with the median peak amplitude; (h) spectra of the seismograms from (g).

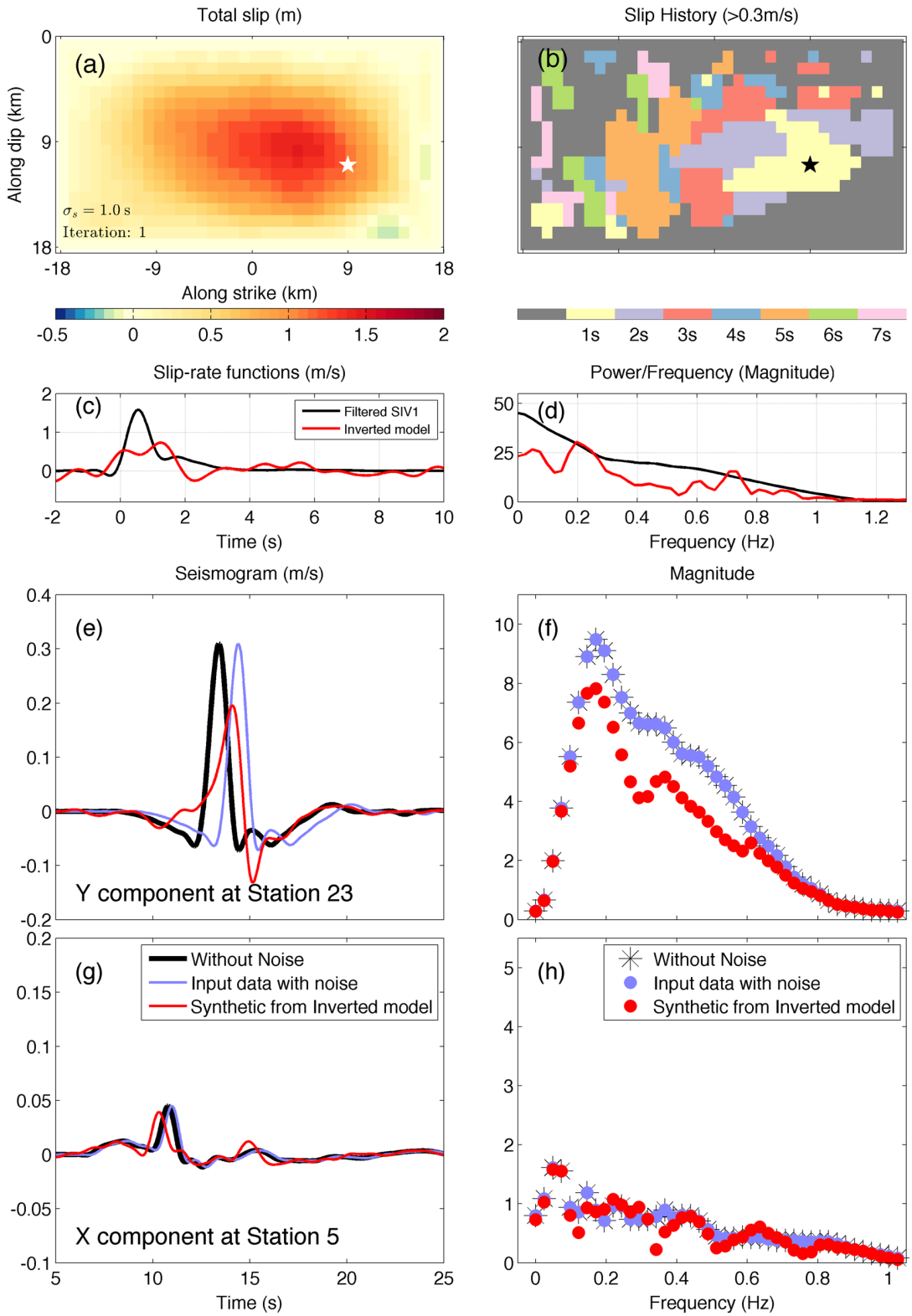

Figure 17. Inverted source model from data with time-shift errors ($\sigma_s = 1$ s), solved by regularization without iteration. (a) Total slip; (b) slip history; (c) slip-rate function at hypocentre; (d) spectrum of the slip-rate function; (e) seismograms with the largest peak amplitude; (f) spectra of the seismograms from (e); (g) seismogram with the median peak amplitude; (h) spectra of the seismograms from (g).

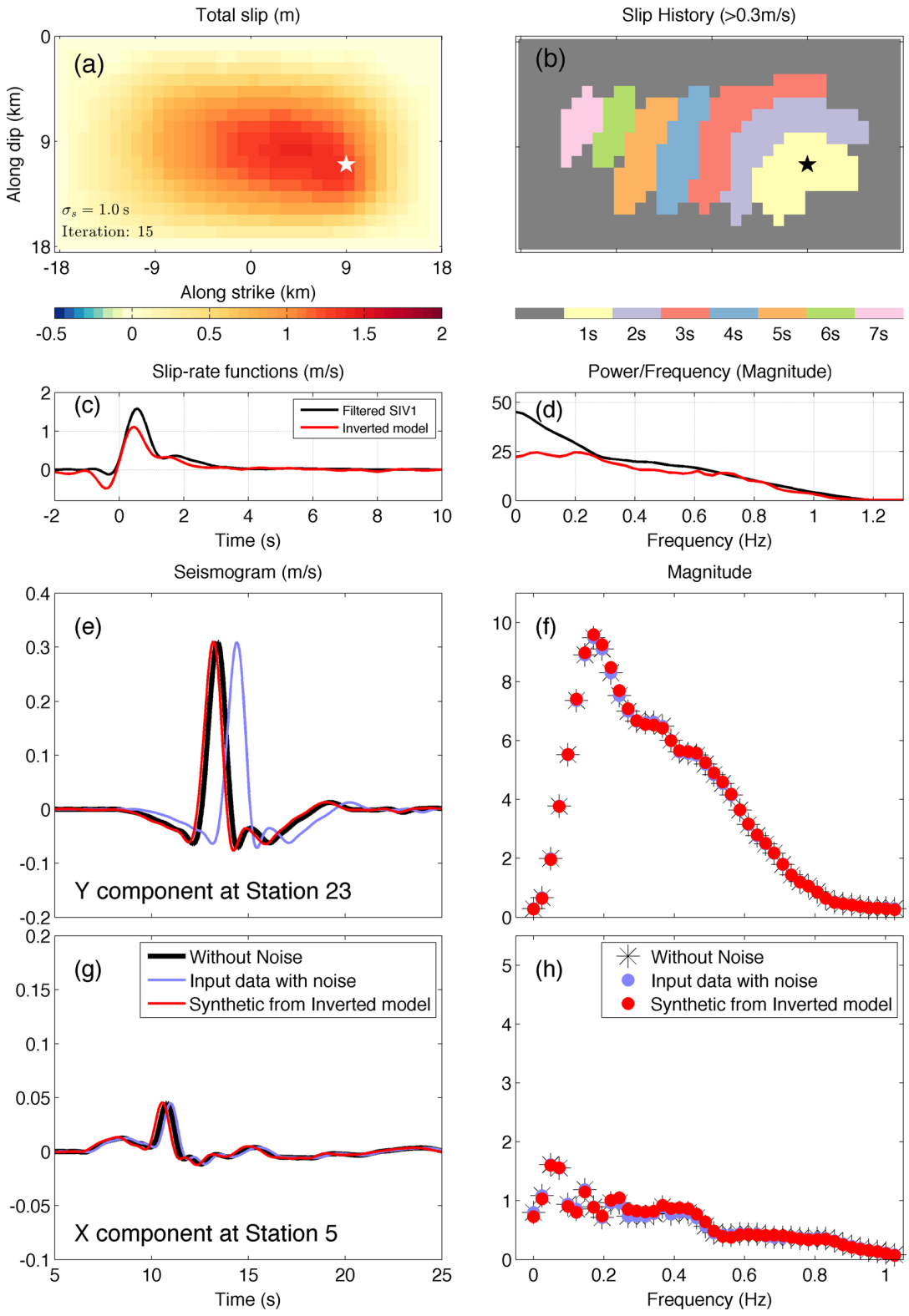

Figure 18. Inverted source model from data with time-shift errors ($\sigma_s = 1$ s) after 15 iterations to correct for time-shift errors. (a) Total slip; (b) slip history; (c) slip-rate function at hypocentre; (d) spectrum of the slip-rate function; (e) seismograms with the largest peak amplitude; (f) spectra of the seismograms from (e); (g) seismogram with the median peak amplitude; (h) spectra of the seismograms from (g).

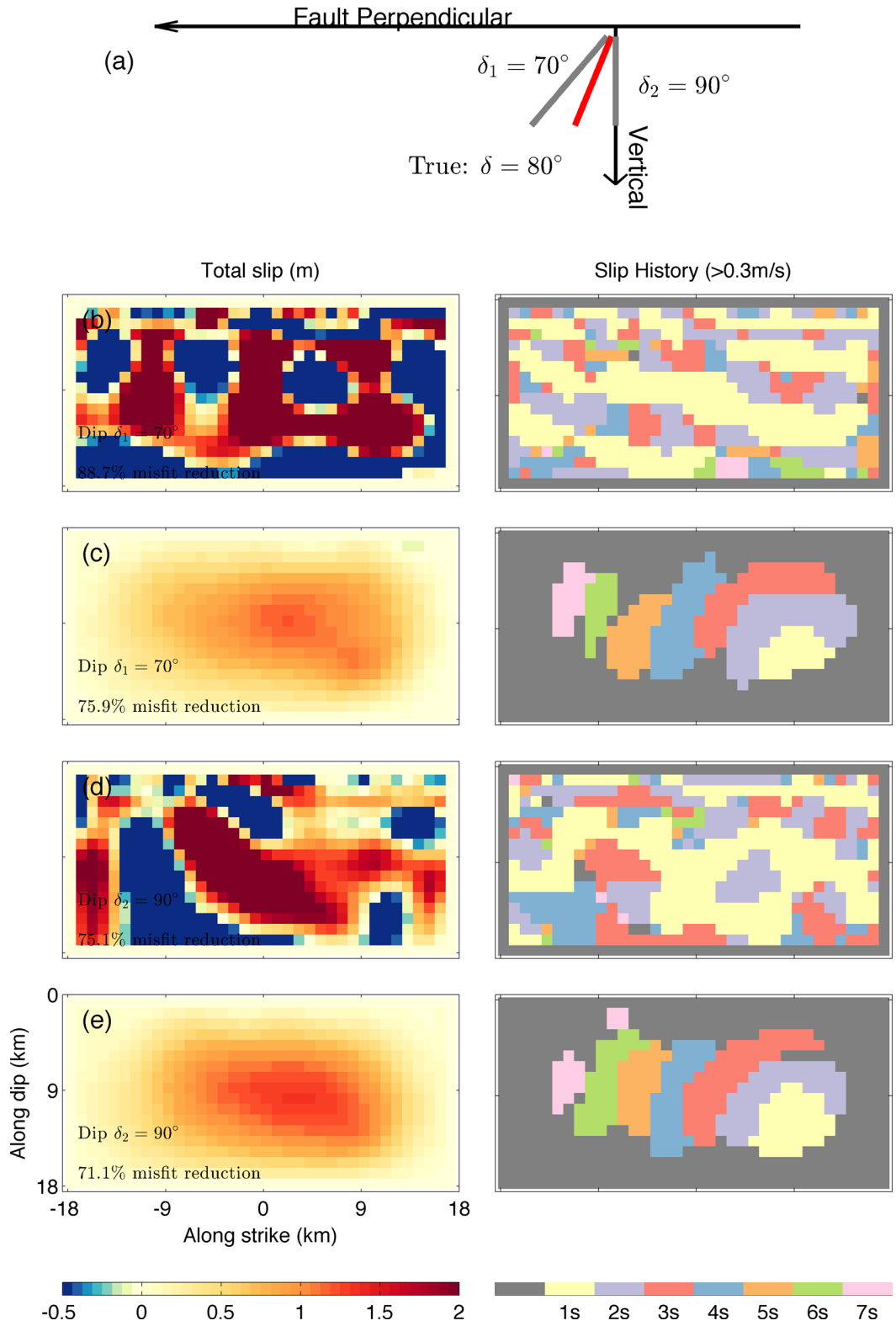

Figure 19. Inverted source models with assumed fault dips. (a) Assumed fault geometry; (b) total slip and slip history for $\delta_1 = 70°$ with the same regularization strength as the preferred model. (c) Total slip and slip history for $\delta_1 = 70°$ with strong regularization strength. (d) Total slip and slip history for $\delta_2 = 90°$ with the same regularization strength as the preferred model. (e) Total slip and slip history for $\delta_2 = 90°$ with strong regularization strength.

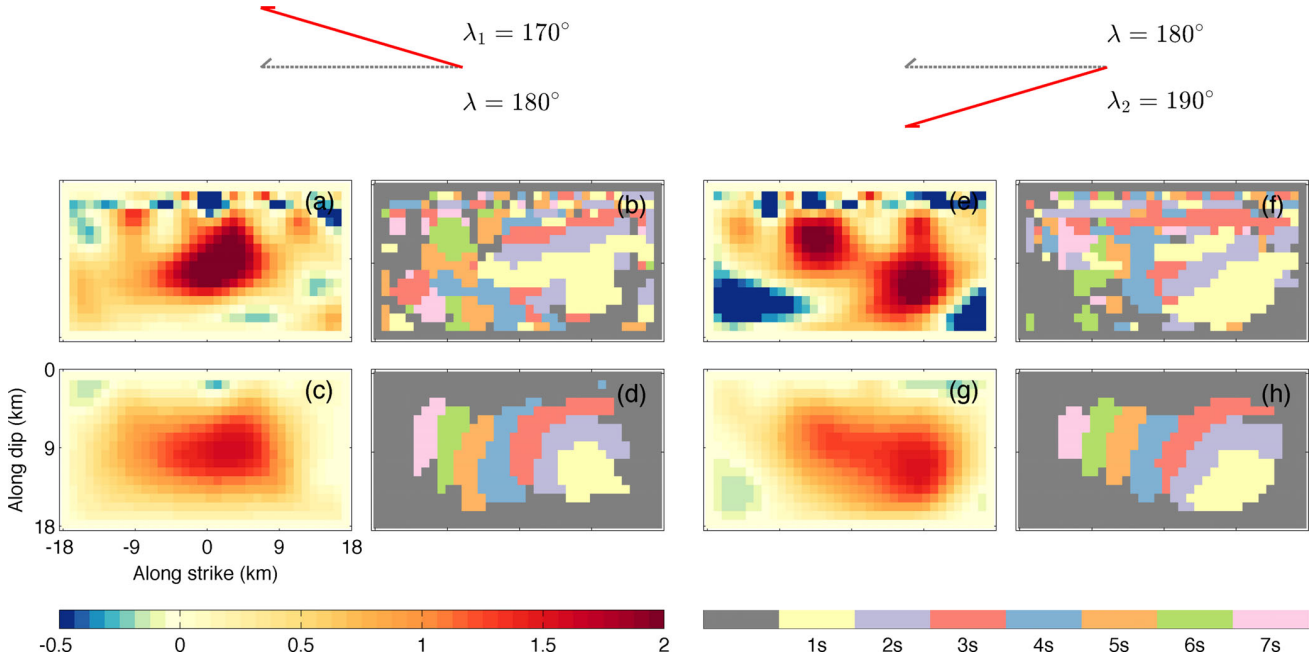

Figure 20. Inverted source models with assumed rakes, true rake $\lambda = 180^\circ$. Panels (a)–(d), assumed rake $\lambda_1 = 170^\circ$, (a) and (b) show total slip and slip history with the same regularization strength as the preferred model. Panels (c) and (d) show total slip and slip history with strong regularization strength. Panels (e)–(h) assumed rake $\lambda_2 = 190^\circ$; (e) and (f) show total slip and slip history with the same regularization strength as the preferred model. Panels (g) and (h) show total slip and slip history with strong regularization strength.

Green's functions for the erroneous fault location for the inversion, while using data generated using the true 80° dipping fault.

For unchanged regularization, using the wrong fault dip severely affects our solutions, generally having much worse effects than the random Gaussian noise or time-shift errors. The models obtained using the same relatively weak regularization as before are quite heterogeneous and bear little resemblance to the true models, particularly for the slip time histories (see Fig. 19), while achieving relatively poor data fits of 88.7 and 75.1 per cent misfit reduction for the 70° and 90° models, respectively (Table 1). For the same σ_m^2, taking the unknown fault geometry into account, σ^2 will increase, which will lead to an increase in α^2 and λ^2 (eqs 9 and 12). Increasing the regularization strength can produce more plausible appearing models and slip histories. Of course, for real problems, where we do not know the true model, it would be difficult to determine the optimal level of regularization.

A likely reason that errors in the assumed fault dip have such a large impact is that they introduce correlated errors, that is they cause arrivals to be systematically early on one side of the fault compared to the other. This same kind of error may also occur from unmodelled large-scale velocity variations, for example if velocities were faster on one side of the fault and this was not taken into account (e.g. Gallovič *et al.* 2010). Another more serious problem is the rotation of the radiation pattern from its correct orientation causing the amplitude and even the polarity of some arrivals to be incorrect. To address these difficulties it might make sense to include the fault orientation as part of the inversion. However, this would make the problem non-linear and we not yet experimented with the feasibility of this approach.

5.2.2 Unknown rake

Rake can be taken as an unknown parameter in source inversion (e.g. Ji *et al.* 2002). To stabilize the inversion, it can also be specified for each subfault (e.g. Yue *et al.* 2012). Until now we have used the true rake for all our inversions. To analyse the errors introduced by possible inaccurately known rake, we perform inversions with two specified rakes (±10° of the true one), while dip is fixed to be the same as SIV1 (see Fig. 20).

For unchanged regularization, the wrong fault rake strongly affects our solutions. The effects are similar to those from using the wrong dip. The models obtained using the same relatively weak regularization as before have large negative slip areas, and no clear pattern can be observed from slip-time histories (see Fig. 19), while fitting data with 94.8 and 94.0 per cent misfit reduction for the 170° and 190° models, respectively (Table 1). Similar to the unknown dip situation, the wrong rake will lead to an increase in α^2 and λ^2 (eqs 9 and 12). Increasing the regularization strength can produce more plausible appearing models and slip histories, but with poor data fit (Table 1). It is difficult to decide on the appropriate regularization strength based on the L-curve for the unknown fault geometry cases, because subjective evaluation is needed to pick the right model besides considering the data misfit and model size.

6 CONCLUSIONS

We have developed a frequency-based source-inversion method that makes fewer assumptions than most current methods and applied it to SIV Exercise 1. We find that various physically plausible regularizations obtain robust inversion results. We spatially overparametrize the model (1 km × 1 km) to avoid errors from too few unknowns. The linear relationship between slip-rate spectra and recorded spectra guarantees finding the global misfit minimum when convex optimization is applied to solve the inversion. Many details of the rupture process can be recovered reasonably well by the method, including rupture velocity and slip-rate functions.

Advantages of the frequency domain approach compared to time domain slip inversion algorithms are: (1) it is fundamentally linear

and does not require any limits on the rupture velocity or duration of the slip function. Thus in principle, it should be able to resolve complicated ruptures, including variable rupture speeds, and even reversals of rupture direction, although these complexities were not analysed. (2) Because it operates on each frequency separately, the complexity is relatively small and the algorithm is computationally efficient enough to permit a very fine spatial sampling of the fault and testing different regularizations.

The main disadvantage of the frequency domain method is that it is less direct than the time domain methods, which makes it more difficult to impose physically plausible constraints on slip direction and timing. In particular, we do not apply a positivity constraint on fault slip or prohibit slip at times earlier than the *P*-wave arrival from the hypocentre. However, static corrections, as shown in Section 5.1.3. can obtain coherent solutions around the hypocentre near the origin time. For the synthetic examples, regularization reduces negative slip and acausal slip to almost negligible amplitude and physically plausible constrains are not needed. However, physically unrealistic slip may well prove a bigger problem for inversions of real earthquakes.

Aiming to provide an improved understanding of the resolution limits and uncertainties in kinematic source inversions, we explored the robustness of the method with respect to noise, timing errors and unknown fault geometry. Random Gaussian noise does not have a severe effect on the inverted source model, provided enough stations are available to effectively average it out. Random time-shifts caused by station timing errors or poorly known Green's functions can strongly damage the inversion, but can effectively be removed using an iterative approach that involves cross-correlation of data and synthetics, provided the time-shifts are random and uncorrelated. A more severe problem is uncertainties in the assumed fault geometry. Errors in the fault dip and rake angle of 10° requires stronger regularization strength to produce more reasonable models, which are still relatively poorly resolved.

ACKNOWLEDGEMENTS

We thank Martin Mai for the SIV1 exercise and Paul Spudich for the COMPSYN software package. This work was supported by grants from the National Science Foundation EAR1111111, EAR-0710881 and EAR-0944109. The authors thank two anonymous reviewers and the editor for suggestions that improved the quality of this manuscript.

REFERENCES

Aki, K. & Richards, P.G., 2002. *Quantitative Seismology,* University Science Books.

Allmann, B.P. & Shearer, P.M., 2007. A high-frequency secondary event during the 2004 Parkfield earthquake, *Science,* **318**(5854), 1279–1283.

Boyd, S.P. & Vandenberghe, L., 2004. *Convex Optimization,* Cambridge University Press.

Causse, M., Dalguer, L.A. & Mai, P.M., 2014. Variability of dynamic source parameters inferred from kinematic models of past earthquakes, *Geophys. J. Int.,* **196**(3), 1754–1769.

Claerbout, J.F. & Fomel, S., 2008. Image estimation by example: geophysical soundings image construction: multidimensional autoregression, http://sepwww.stanford.edu/sep/prof/.

Cormier, V.F., 2007. Theory and observations-forward modeling/synthetic body wave seismograms, in *Treatise on Geophysics,* pp. 157–189, ed. Schubert, G., Elsevier.

Cotton, F. & Campillo, M., 1995. Frequency domain inversion of strong motions: application to the 1992 Landers earthquake, *J. geophys. Res.,* **100**(B3), 3961–3975.

Dettmer, J., Benavente, R., Cummins, P.R. & Sambridge, M., 2014. Trans-dimensional finite-fault inversion, *Geophys. J. Int.,* **199**(2), 735–751.

Ely, G.P., Day, S.M. & Minster, J.-B., 2008. A support-operator method for viscoelastic wave modelling in 3-D heterogeneous media, *Geophys. J. Int.,* **172**(1), 331–344.

Ely, G.P., Day, S.M. & Minster, J.-B., 2009. A support-operator method for 3-D rupture dynamics, *Geophys. J. Int.,* **177**(3), 1140–1150.

Fukahata, Y., Yagi, Y. & Rivera, L., 2014. Theoretical relationship between back-projection imaging and classical linear inverse solutions, *Geophys. J. Int.,* **196**(1), 552–559.

Gallovič, F. & Zahradník, J., 2012. Complexity of the Mw 6.3 2009 L'aquila (central Italy) earthquake: 1. Multiple finite-extent source inversion, *J. geophys. Res.: Solid Earth,* **117**(B4), doi:10.1029/2011JB008709.

Gallovič, F., Käser, M., Burjánek, J. & Papaioannou, C., 2010. Three-dimensional modeling of near-fault ground motions with nonplanar rupture models and topography: case of the 2004 Parkfield earthquake, *J. geophys. Res.: Solid Earth,* **115**(B3), doi:10.1029/2008JB006171.

Grant, M. & Boyd, S., 2008. Graph implementations for nonsmooth convex programs, in *Recent Advances in Learning and Control,* Lecture Notes in Control and Information Sciences, pp. 95–110, eds Blondel, V., Boyd, S. & Kimura, H., Springer-Verlag Limited.

Grant, M. & Boyd, S., 2013. CVX: Matlab software for disciplined convex programming, version 2.0 beta, http://cvxr.com/cvx.

Hartzell, S.H. & Heaton, T.H., 1983. Inversion of strong ground motion and teleseismic waveform data for the fault rupture history of the 1979 Imperial Valley, California, earthquake, *Bull. seism. Soc. Am.,* **73**(6A), 1553–1583.

Haskell, N.A., 1969. Elastic displacements in the near-field of a propagating fault, *Bull. seism. Soc. Am.,* **59**(2), 865–908.

Ide, S., 2007. Slip inversion, *Treatise on Geophysics,* pp. 193–223, ed. Schubert, G., Elsevier.

Ji, C., Wald, D.J. & Helmberger, D.V., 2002. Source description of the 1999 Hector Mine, California, earthquake. Part I: wavelet domain inversion theory and resolution analysis, *Bull. seism. Soc. Am.,* **92**(4), 1192–1207.

Koketsu, K., Hikima, K., Miyazaki, S. & Ide, S., 2004. Joint inversion of strong motion and geodetic data for the source process of the 2003 Tokachi-oki, Hokkaido, earthquake, *Earth Planets Space,* **56**(3), 329–334.

Koketsu, K. *et al.*, 2011. A unified source model for the 2011 Tohoku earthquake, *Earth planet. Sci. Lett.,* **310**(3–4), 480–487.

Konca, A.O., Kaneko, Y., Lapusta, N. & Avouac, J.-P., 2013. Kinematic inversion of physically plausible earthquake source models obtained from dynamic rupture simulations, *Bull. seism. Soc. Am.,* **103**(5), 2621–2644.

Maercklin, N., Festa, G., Colombelli, S. & Zollo, A., 2012. Twin ruptures grew to build up the giant 2011 Tohoku, Japan, earthquake., *Scientific Reports,* **2,** 709, doi:10.1038/srep00709.

Mai, P.M., 2013. Uncertainty quantification in earthquake source inversions: the source inversion validation (SIV) project, in *Proceedings of the EGU General Assembly Conference,* Abstracts, Vol. 15, p. 3596.

Mai, P., Burjanek, J., Delouis, B., Festa, G., Francois-Holden, C., Monelli, D., Uchide, T. & Zahradnik, J., 2007. Earthquake source inversion blindtest: initial results and further developments, *EOS, Trans. Am. geophys. Un.,* **88**(52), Fall Meet. Suppl., Abstract S53C-08.

Mendez, A.J. & Anderson, J.G., 1991. The temporal and spatial evolution of the 19 September 1985 Michoacán earthquake as inferred from near-source ground-motion records, *Bull. seism. Soc. Am.,* **81**(3), 844–861.

Minson, S.E., Simons, M. & Beck, J.L., 2013. Bayesian inversion for finite fault earthquake source models. I—theory and algorithm, *Geophys. J. Int.,* **194**(3), 1701–1726.

Minson, S.E. *et al.*, 2014. Bayesian inversion for finite fault earthquake source models. II— the 2011 great Tohoku-Oki, Japan earthquake, *Geophys. J. Int.,* **198**(2), 922–940.

Monelli, D. & Mai, P.M., 2008. Bayesian inference of kinematic earthquake rupture parameters through fitting of strong motion data, *Geophys. J. Int.,* **173**(1), 220–232.

Monelli, D., Mai, P.M., Jónsson, S. & Giardini, D., 2009. Bayesian imaging of the 2000 Western Tottori (Japan) earthquake through fitting of strong motion and GPS data, *Geophys. J. Int.,* **176**(1), 135–150.

Olson, A.H. & Anderson, J.G., 1988. Implications of frequency-domain inversion of earthquake ground motions for resolving the space-time dependence of slip on an extended fault, *Geophys. J. Int.,* **94**(3), 443–455.

Olson, A.H. & Apsel, R.J., 1982. Finite faults and inverse theory with applications to the 1979 Imperial Valley earthquake, *Bull. seism. Soc. Am.,* **72**(6A), 1969–2001.

Page, M., Mai, P.M. & Schorlemmer, D., 2011. Testing earthquake source inversion methodologies, *EOS, Trans. Am. geophys. Un.,* **92**(9), 75–75.

Razafindrakoto, H.N.T. & Mai, P.M., 2014. Uncertainty in earthquake source imaging due to variations in source time function and Earth structure, *Bull. seism. Soc. Am.,* **104,** 855–874.

Shao, G. & Ji, C., 2012. What the exercise of the SPICE source inversion validation blindtest 1 did not tell you, *Geophys. J. Int.,* **189**(1), 569–590.

Spudich, P. & Archuleta, R.J., 1987. Techniques for earthquake ground-motion calculation with applications to source parameterization of finite faults, in *Seismic Strong Motion Synthetics, Computational Techniques,* pp. 205–265, ed. Bolt, B., Academic Press.

Tong, X., Sandwell, D.T. & Fialko, Y., 2010. Coseismic slip model of the 2008 Wenchuan earthquake derived from joint inversion of interferometric synthetic aperture radar, GPS, and field data, *J. geophys. Res.,* **115**(B4), doi:10.1029/2009JB006625.

Trifunac, M.D., 1974. A three-dimensional dislocation model for the San Fernando, California, earthquake of February 9, 1971, *Bull. seism. Soc. Am.,* **64**(1), 149–172.

Uchide, T., Ide, S. & Beroza, G.C., 2009. Dynamic high-speed rupture from the onset of the 2004 Parkfield, California, earthquake, *Geophys. Res. Lett.,* **36**(4), doi:10.1029/2008GL036824.

Vallée, M. & Bouchon, M., 2004. Imaging coseismic rupture in far field by slip patches, *Geophys. J. Int.,* **156**(3), 615–630.

Xenaki, A., Gerstoft, P. & Mosegaard, K., 2014. Compressive beamforming, *J. acoust. Soc. Am.,* **136**(1), doi:10.1121/1.4883360.

Yagi, Y., 2004. Source rupture process of the 2003 Tokachi-oki earthquake determined by joint inversion of teleseismic body wave and strong ground motion data, *Earth planet. Sci.,* **56**(3), 311–316.

Yagi, Y. & Fukahata, Y., 2011. Introduction of uncertainty of Green's function into waveform inversion for seismic source processes, *Geophys. J. Int.,* **186**(2), 711–720.

Yao, H., Gerstoft, P., Shearer, P.M. & Mecklenbräuker, C., 2011. Compressive sensing of the Tohoku-Oki Mw 9.0 earthquake: frequency-dependent rupture modes, *Geophys. Res. Lett.,* **38**(20), doi:10.1029/2011GL049223.

Yokota, Y., Koketsu, K., Fujii, Y., Satake, K., Sakai, S., Shinohara, M. & Kanazawa, T., 2011. Joint inversion of strong motion, teleseismic, geodetic, and tsunami datasets for the rupture process of the 2011 Tohoku earthquake, *Geophys. Res. Lett.,* **38**(7), doi:10.1029/2011GL050098.

Yue, H., Lay, T. & Koper, K.D., 2012. En echelon and orthogonal fault ruptures of the 11 April 2012 great intraplate earthquakes, *Nature,* **490**(7419), 245–249.